CHEMISTRY OF MATERIALS
Article
Cite This: Chem. Mater. 2019, 31, 2661−2676
pubs.acs.org/cm

Syntheses of Colloidal $F:In_2O_3$ Cubes: Fluorine-Induced Faceting and Infrared Plasmonic Response

Shin Hum Cho,[†,#] Sandeep Ghosh,[†,#] Zachariah J. Berkson,[§,#] Jordan A. Hachtel,[∥] Jianjian Shi,[‡] Xunhua Zhao,[‡] Lauren C. Reimnitz,[†] Clayton J. Dahlman,[†,⊥] Yujing Ho,[†] Anni Yang,[†] Yuanyue Liu,[‡] Juan-Carlos Idrobo,[∥] Bradley F. Chmelka,[*,§] and Delia J. Milliron[*,†]

[†]McKetta Department of Chemical Engineering and [‡]Texas Materials Institute and Department of Mechanical Engineering, The University of Texas at Austin, Austin, Texas 78712, United States

[§]Department of Chemical Engineering, University of California, Santa Barbara, Santa Barbara, California 93106, United States

[∥]Center for Nanophase Materials Science, Oak Ridge National Laboratory, Oak Ridge, Tennessee 37831, United States

[⊥]Materials Department, University of California, Santa Barbara, Engineering II Building 1355, Santa Barbara, California 93106-5050, United States

S *Supporting Information*

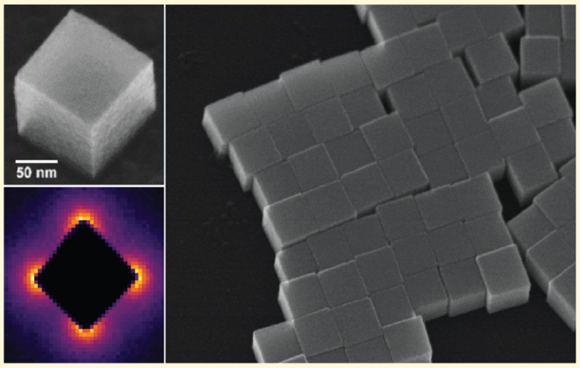

ABSTRACT: Cube-shaped nanocrystals (NCs) of conventional metals like gold and silver generally exhibit localized surface plasmon resonance (LSPR) in the visible region with spectral modes determined by their faceted shapes. However, faceted NCs exhibiting LSPR response in the infrared (IR) region are relatively rare. Here, we describe the colloidal synthesis of nanoscale fluorine-doped indium oxide ($F:In_2O_3$) cubes with LSPR response in the IR region, wherein fluorine was found to both direct the cubic morphology and act as an aliovalent dopant. Single-crystalline 160 nm $F:In_2O_3$ cubes terminated by (100) facets and concave cubes were synthesized using a colloidal heat-up method. The presence of fluorine was found to impart higher stabilization to the (100) facets through density functional theory calculations that evaluated the energetics of F-substitution at surface oxygen sites. These calculations suggest that the cubic morphology results from surface binding of F atoms. In addition, fluorine acts as an anionic aliovalent dopant in the cubic bixbyite lattice of In_2O_3, introducing a high concentration of free electrons leading to LSPR. We confirmed the presence of lattice fluorine dopants in these cubes using solid-state ^{19}F and ^{115}In nuclear magnetic resonance spectroscopy. The cubes exhibit narrow, shape-dependent multimodal LSPR extinction peaks due to corner- and edge-centered modes. The spatial origin of these different contributions to the spectral response is directly visualized by electron energy loss spectroscopy in a scanning transmission electron microscope.

■ INTRODUCTION

Colloidal syntheses of doped metal oxide nanocrystals (NCs) have emerged recently as new means of extending localized surface plasmon resonance (LSPR) to the infrared (IR) range,[1] although shape control is yet to be broadly established.[2] A wide range of morphologies have been reported for colloidal gold and silver NCs,[3] including cubes[4,5] and octopods,[6] leading to the observation of shape-dependent LSPR and strongly enhanced electromagnetic near-fields around corners and edges. Yet, metal NCs intrinsically possess high free carrier concentrations exceeding 10^{23} cm^{-3} so the optical response of isotropic NCs tends to be restricted to the visible region of the electromagnetic spectrum.[7,8] On the other hand, controlled doping of semiconductor NCs allows lower carrier concentrations around 10^{21} cm^{-3}, resulting in IR-range LSPR.[9,10] In this study, we demonstrate shape-controlled colloidal syntheses of highly faceted, fluorine-doped indium oxide ($F:In_2O_3$) cubes with an LSPR response in the IR range.

Typically, doping strategies in plasmonic metal oxide NCs (e.g., $Sn:In_2O_3$,[11] Al:ZnO,[12] and In:CdO[13] NCs) have focused on aliovalent cation substitution. Halogen anions, meanwhile, can act as surface capping agents[14] that have been used for shape control of metal,[15] metal oxide,[16] and metal chalcogenide[17,18] NCs. In some metal oxide NCs, fluorine has been incorporated as an anionic co-dopant (e.g., F,In:CdO,[19] $F,Sn:In_2O_3$[20]). Very little has been reported regarding fluorine doping alone to induce LSPR, as in fluorinated TiO_2 NCs.[21] Furthermore, whereas anionic doping in nanocrystalline $F:SnO_2$ has been demonstrated, the effects of fluorine on faceting or LSPR properties of metal oxide NCs have not been well explored.[22] A comprehensive material characterization is yet needed to simultaneously unravel the

Received: March 5, 2019
Revised: March 11, 2019
Published: March 21, 2019

role of fluorine in LSPR-inducing internal doping and shape-inducing surface faceting effect for metal oxide NCs.

Faceted NCs give rise to shape-dependent LSPR phenomena not observed for spherical NCs, including highly enhanced near-field hot spots around corners and edges[23] that, in conventional metals, have been leveraged for plasmonic nanoantennae[24,25] and surface-enhanced Raman spectroscopy.[26,27] Shape effects and the understanding of plasmonic behavior have advanced in other classes of non-noble metal plasmonic materials, such as copper chalcogenides,[28,29] and been extended in refractory metal nitrides.[8,30,31] Disks and elongated NCs of copper chalcogenides have been reported in shape effects on their LSPR properties,[29] which are likely to be strongly influenced by crystalline anisotropy as well.[32] Yet, shape-dependent studies of LSPR specific to doped metal oxide NCs are few,[13,32] motivating the development of new strategies for synthetic shape control, as large cube NC sizes,[20] and well-defined corners[10] can lead to higher magnitude in near-field enhancement for doped metal oxide NCs. Focal to this work, access to larger NC sizes with larger volume-to-surface ratios allow F:In_2O_3 NCs to be model materials in decoupling the roles of internal fluorine dopants and surface fluorine, supported by extensive material characterization and high spatial resolution for single-particle analysis.

We succeed in modulating the shape of F:In_2O_3 NCs by varying the ratio of InF_3 to In(acac)$_3$ precursors and observe multimodal shape-dependent LSPR extinction features. The role of fluorine in defining NC facets and inducing LSPR spectral response is attributed to the presence of fluorine on the external surfaces and internally within the NCs, respectively. Through X-ray photoelectron spectroscopy (XPS) and solid-state ^{19}F magic-angle-spinning (MAS) nuclear magnetic resonance (NMR) spectroscopy correlated with density functional theory (DFT) calculations, fluorine is found to occupy surface sites on dominantly exposed {100} facets. Fluorine dopant species internal to the NCs are probed by X-ray diffraction (XRD), energy dispersive X-ray (EDX) spectroscopy, time of flight secondary ion mass spectrometry (TOF-SIMS), and ^{19}F MAS-NMR spectroscopy. Aliovalent substitutional fluorine doping on oxygen lattice sites leads to free carrier compensation, inducing LSPR. The local metallic environments of the subsurface fluorine and indium atoms in the NC lattices are established by analyses of ^{19}F spin-lattice T_1 relaxation times and wideline ^{115}In NMR spectra, which are shown to exhibit temperature and frequency dependencies that are characteristic of coupling to free (metallic) electron carriers. Arising from the free carriers and highly faceted NC shape, single-NC LSPR spatial modes are directly visualized by monochromated electron energy loss spectroscopy (EELS) performed in a scanning transmission electron microscope (STEM) to assign the observed multimodal features to distinct spatial dipolar modes. The observed material characteristics lead to IR light near-field localization, making F:In_2O_3 NCs a foundation material for near-field enhancement applications in IR.

■ EXPERIMENTAL METHODS

Materials. Indium(III) acetylacetonate (In(acac)$_3$, 99.99%), indium(III) fluoride (InF_3, >99.9%), indium(III) chloride ($InCl_3$, 99.999%), indium(III) bromide ($InBr_3$, 99.999%), oleic acid (OA, 90%, technical grade), octylamine (OcAm, 99%), trioctylamine (TOA, 98%), and tetrachloroethylene (TCE, ≥99%) were purchased from Sigma-Aldrich. Toluene (99.5%) was purchased from Fisher Chemical. All chemicals were used as received without any further purification.

Fluorine-Doped Indium Oxide (F:In_2O_3) Cube (3% InF_3) Synthesis. All synthesis procedures were carried out using standard Schlenk line techniques aided by a nitrogen-filled glovebox. For the growth of 3% doped F:In_2O_3 cubes, a mixture of In(acac)$_3$ (399.78 mg, 0.97 mmol), InF_3 (5.15 mg, 0.03 mmol), OA (1 mL), OcAm (0.5 mL), and TOA (3.5 mL) was loaded in a three-neck round-bottom flask in the glovebox. This precursor mixture was then stirred with a magnetic bar at 600 rpm and degassed under vacuum at 120 °C for 15 min. The mixture turned transparent during this operation, signifying the formation of indium oleate (In-OA). Thereafter, the flask was filled with nitrogen and further heated at a ramp rate of 15 °C/min to 320 °C. The reaction mixture turned cloudy and opaque, which signified cube growth and was designated as the growth reaction start time. The growth reaction was allowed to run for 5 min at 320 °C or the desired set point temperature. Subsequently, growth was terminated by removing the heating mantle and the reaction mixture was cooled by blowing an air jet on the flask. The cubes were washed and dispersed in toluene and centrifuged at 4500 rpm for 5 min. This washing process was repeated three times. The resultant cubes were redispersed in toluene for further analysis.

Varying concentrations of F doping in these NCs were achieved by controlling the molar ratio of InF_3 to In(acac)$_3$, while keeping other reaction parameters identical. Aliquots (0.1 mL), at various reaction times during growth, were extracted from the reaction mixture with a nitrogen-purged syringe needle and quenched into TCE for further analysis.

Indium Oxide (In_2O_3) NC Synthesis. Undoped indium oxide (In_2O_3) NCs were synthesized by adding In(acac)$_3$ (1 mmol) in the reaction flask without InF_3 while keeping other reaction parameters identical to the procedure described above for the F-doped NCs.

Chlorine/Bromine-Doped Indium Oxide (Cl:In_2O_3, Br:In_2O_3) NC Synthesis. Cl:In_2O_3 (3% $InCl_3$) NCs were synthesized by adding In(acac)$_3$ (0.97 mmol), substituting $InCl_3$ (0.03 mmol) precursor for InF_3 in the reaction flask, while keeping other reaction parameters identical. In a similar manner, $InBr_3$ (0.03 mmol) was used to synthesize Br:In_2O_3 (3% $InBr_3$) NCs, keeping other reaction parameters identical.

Fourier Transform IR (FTIR) Spectra. FTIR spectral measurements were conducted using a Bruker Vertex 70 FTIR at 4 cm^{-1} resolution. Aliquot solutions were diluted in TCE and loaded into a liquid cell with KBr windows for FTIR measurements. NCs dispersed in TCE were sonicated for 1 h to prevent aggregation before loading into the liquid cell.

XRD Analysis. Samples for XRD measurements were prepared by drop-casting a 10 mg/mL dispersion of F:In_2O_3 NCs on silicon substrates. The data were collected with a Rigaku MiniFlex 600 X-ray diffractometer using Cu Kα radiation, 1.54 Å, and analyzed with GSAS-II software.[33]

Electron Microscopy. Samples were prepared by drop-casting NC dispersions onto carbon-coated 400 mesh copper grids (Ted Pella), and the imaging was performed in a Hitachi S5500 scanning electron microscope (SEM) operating in the STEM mode at an accelerating voltage of 30 kV. NC size analysis was performing with ImageJ software with 250 NC count. High-resolution transmission electron microscopy (HRTEM) images and selected-area electron diffraction (SAED) patterns were acquired with a JEOL 2010F transmission electron microscope (TEM) equipped with a charge-coupled device camera and a Schottky field emission gun operating at 200 kV.

Elemental Analysis. Elemental spectrum acquisition of F:In_2O_3 cubes drop-cast on silicon substrates was carried out using a Hitachi S5500 SEM with a Bruker XFlash EDX detector attachment at 5 kV. Elemental deconvolution was performed with the Bruker Quantax software reference library at zero-tilt angle P/B-ZAF correction. TOF-SIMS was conducted on TOF.SIMS 5, ION-TOF GmbH with Cs$^+$ sputtering at 2 kV.

Thermogravimetric Analysis (TGA). Measurements were carried out using a Mettler Toledo TGA2 thermogravimetric analyzer.

Dried NC powders were loaded into alumina crucibles of 100 μL volume and heated from 25 to 1100 °C at a heating rate of 5 °C/min under nitrogen flow (50 sccm).

XPS. Samples were prepared by drop casting NC solutions on silicon substrates, and the measurements were performed in a Kratos Axis Ultra DLD spectrometer with a monochromatic Al Kα source (1486.6 eV). Wide survey scans were acquired at analyzer pass energy of 80 eV, and the high-resolution narrow region scans were performed at a pass energy of 20 eV with steps of 0.1 eV. Spectral acquisitions were performed with photoelectron take-off angle at 0° with respect to the surface normal, and pressure in the analysis chamber was maintained at around 10^{-9} Torr. Data analysis was performed in CasaXPS software using the Kratos relative sensitivity factor library. The binding energy (BE) scale was internally referenced to the C 1s peak (BE for C–C = 284.8 eV).

DFT Calculations. DFT calculations were performed using the Vienna Ab initio Simulation Package (VASP)[34,35] with projector augmented wave pseudopotentials[36] in the package. The Perdew–Burke–Ernzerhosf exchange-correlation functional[37] was used in all DFT calculations. A 3 × 3 × 1 Monkhorst–Pack k point mesh for the Brillouin zone integration was used, with a vacuum layer of 15 Å to prevent interactions between periodic images of the slab. Further details are in Text S1, Supporting Information.

Solid-State ^{19}F and ^{115}In NMR Spectroscopy. Solid-state ^{1}H and ^{19}F MAS-NMR spectra were acquired on a Bruker ASCEND 400 MHz (9.4 T) solid-state dynamic nuclear polarization NMR spectrometer operating at Larmor frequencies of 400.202 and 376.532 MHz for ^{1}H and ^{19}F, respectively, and equipped with a variable temperature 2.5 mm triple-resonance H–F–X probehead. For the solid-state MAS-NMR measurements, the F:In_2O_3 NCs were mixed with KBr powder in a 1:1 ratio by mass. The KBr served as an internal temperature probe for accurate determination of the sample temperature under the different measurement conditions.[38,39] The one-dimensional (1D) ^{19}F Hahn echo spectrum was acquired at 35 kHz MAS, at 395 K, and using a 90°-τ-180°-τ pulse sequence with rotor-synchronized τ delay times of one rotor period and 100 kHz radio frequency (rf) pulses. The two-dimensional (2D) ^{1}H{^{19}F} NMR correlation spectrum was acquired by using a 2D dipolar-mediated heteronuclear multiple quantum correlation (HMQC) pulse sequence, where the ^{1}H–^{19}F nuclear dipole–dipole couplings were reintroduced by using SR26$_4$[11] recoupling[40] with 50 kHz rf power for recoupling. The ^{19}F spin-lattice (T_1) relaxation analyses relaxation times at different temperatures were measured by using a saturation-recovery pulse sequence with a Hahn echo detection.

The solid-state ^{115}In NMR spectrum of undoped bulk polycrystalline In_2O_3 (99.9% purity, Aldrich) was acquired on a Bruker AVANCE-III Ultrashield Plus 800 MHz (18.8 T) narrow-bore spectrometer operating at a Larmor frequency of 174.354 MHz for ^{115}In and using a Bruker 3.2 mm broadband double-resonance H-X probehead. The solid-state ^{115}In NMR spectrum of the F:In_2O_3 NCs was acquired on a 19.6 T Bruker DRX NMR spectrometer (National High Magnetic Field Laboratory) operating at a Larmor frequency of 182.266 MHz for ^{115}In and using a custom-built 3.2 mm double resonance H-X probehead. The ^{115}In NMR spectra were acquired using a quadrupolar Carr–Purcell–Meiboom–Gill (QCPMG) pulse sequence,[41] which yields manifolds of very narrow, evenly spaced NMR signals (spikelets), which can be systematically acquired as a series that can be overlaid to map the full central transition (CT) region of the ^{115}In NMR spectra. Each ^{115}In NMR spectrum is presented as a mosaic overlay of 22 individual QCPMG subspectra (plotted in different colors) acquired at evenly spaced frequency intervals. The ^{115}In spectra were referenced to a 1 M $In(NO_3)_3$ solution at 0 ppm. Further details on the ^{19}F and ^{115}In NMR analyses are provided in Text S2, Supporting Information.

STEM-EELS. Plasmon mapping was performed in a Nion high-energy-resolution monochromated EELS STEM at Oak Ridge National Laboratory operated at 60 kV and a Nion prototype spectrometer.[42,43] Using a variable slit we choose an energy resolution of 186 cm^{-1} (23 meV) to optimize the resolution between the plasmon peaks and the signal in the monochromated beam. For the plasmon deconvolution, we use the non-negative matrix factorization (NMF) routine available in the Python HyperSpy library (http://hyperspy.org/). More details can be found in the Supporting Information (Text S3).

RESULTS AND DISCUSSION

NC Shape Control. The shapes of the F:In_2O_3 NCs were controlled by varying the molar ratio of InF_3 to $In(acac)_3$ precursors during synthesis, which also determined the extent of fluorine incorporation in the resulting NCs. F:In_2O_3 NCs with well-defined morphology were produced for 1–3% InF_3 in the growth solution, as shown in Figure 1. SEM images showed that monodisperse NCs (edge length 162.1 ± 9.2 nm) with cubic morphology were obtained exclusively in the presence of InF_3 (3% in the molar ratio to $In(acac)_3$) (Figure 1a, rightmost panel). By comparison, in the absence of InF_3, during the synthesis, NCs with pseudospherical morphology were observed (Figure 1a, leftmost panel), with no cubic-shaped NCs observed. Intermediate amounts of InF_3 led to variations in the NC morphology, specifically forming concave cubes with edges protruding outward for 2% InF_3 (Figure 1a, second from right) and 1% InF_3 (Figure 1a, second from left). The cube morphology persists for higher concentrations of InF_3 (4 and 5%) as well, until a threshold is reached at 6%

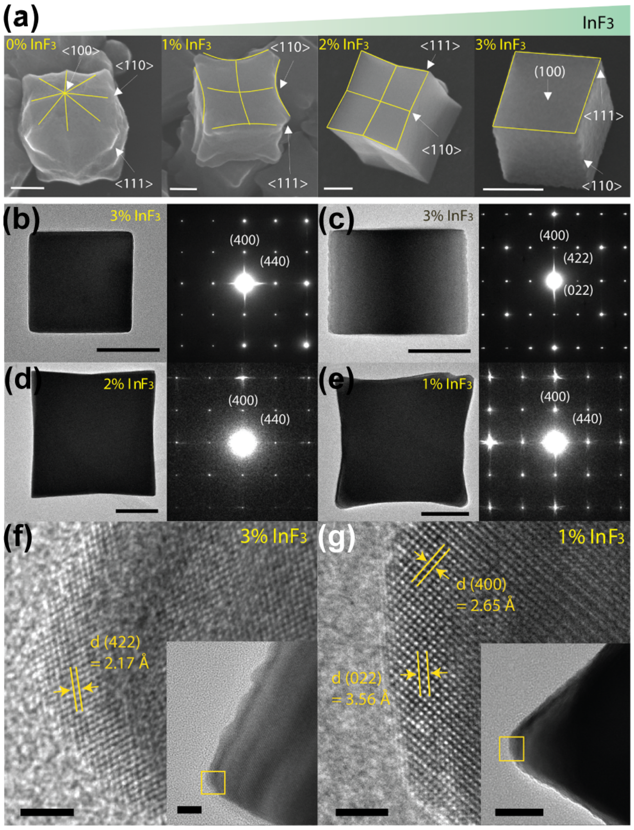

Figure 1. (a) SEM images showing the progressive effect of F on In_2O_3 NC morphology. Outlines are shown as guides to visualize the indicated facets. TEM images (left panels) and the corresponding SAED patterns (right panels) of (b) cube, (c) edge-oriented cube, (d) sharp concave cube, and (e) concave cube F:In_2O_3 NCs. Scale bars are 100 nm for (a)–(e). (f) HRTEM image of a single F:In_2O_3 cube corner with NC oriented on its edge (inset). (g) Extended corner of concave cube F:In_2O_3 NC (inset). Scale bars are 2 nm in (f) and (g) and 20 nm in the insets.

Table 1. EDX Quantification of Fluorine in F:In_2O_3 NCs Synthesized with 1−12% InF_3 Precursor, and Halide Quantification for NCs Synthesized with 3% $InCl_3$ and 3% $InBr_3$ Precursors[a]

sample	precursor $In(acac)_3/InX_3$ (mmol)	initial at. X/In %	measured X/In % (EDX)	measured F/In % (TOF-SIMS)
1% InF_3	0.99:0.01	3.0	6.65 ± 0.48	2.7
2% InF_3	0.98:0.02	6.0	8.56 ± 1.59	9.2
3% InF_3	0.97:0.03	9.0	11.76 ± 2.70	10.3
6% InF_3	0.94:0.06	18.0	26.40 ± 0.36	22.7
12% InF_3	0.88:0.12	36.0	30.58 ± 2.40	30.6
3% $InCl_3$	0.97:0.03	9.0	0.32 ± 0.11	
3% $InBr_3$	0.97:0.03	9.0	2.62 ± 0.06	

[a] The EDX fluorine quantification in F:In_2O_3 NCs is accompanied by TOF-SIMS results.

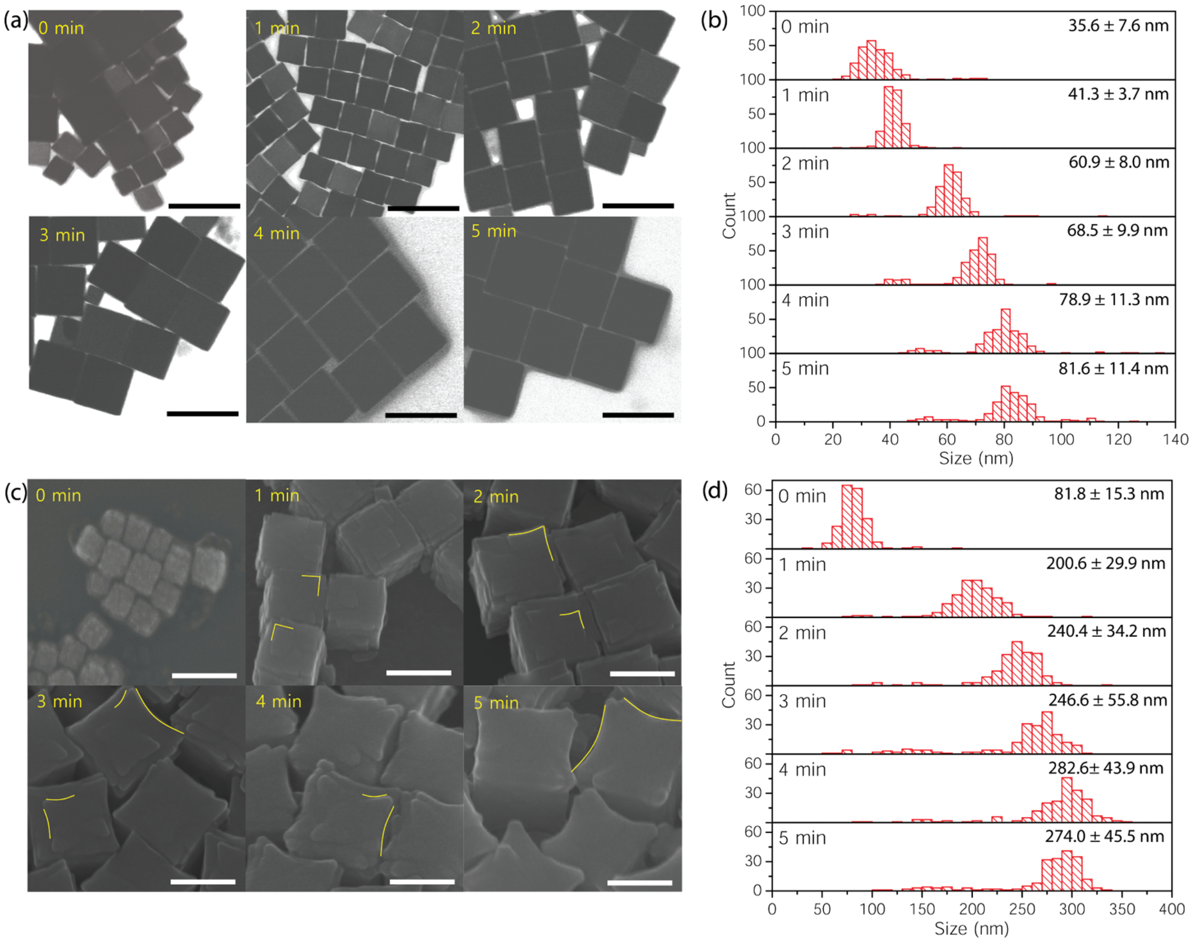

Figure 2. (a) SEM images of aliquots taken at different stages of F:In_2O_3 (3% InF_3) cube synthesis (0−5 min). Scale bars are 100 nm. (b) Size distribution histograms for the corresponding F:In_2O_3 cube aliquots (panel (a)) taken during the growth progression (250 particle count). (c) SEM images of aliquots taken during the growth of F:In_2O_3 (1% InF_3) concave cubes (0−5 min). Yellow lines are drawn as a visual guide to follow the gradual ledge-converging to eventually form the elongated corners. Scale bars at 200 nm. (d) Size distribution histograms for the corresponding F:In_2O_3 concave cube aliquots (panel (c)).

InF_3, beyond which NCs exhibit roughened surfaces (Figure S2).

The TEM images in Figure 1 show that the as-synthesized F:In_2O_3 cubes exhibit well-defined crystalline facets. Selected area electron diffraction (SAED) confirms that the F:In_2O_3 cubes are each single crystals and allows indexing of their surface facets. A TEM image of an F:In_2O_3 cube (3% InF_3) is shown in Figure 1b, which exhibits a flat (100) face and a well-defined edge. The cube is terminated with (100) facets of the In_2O_3 cubic bixbyite structure, corroborated by the position of the (400) reflections in the SAED pattern (Figure 1b, right). A cube on ⟨110⟩ zone axis orientation exhibits (422) reflections in the SAED pattern (Figure 1c, right), corresponding to the (422) spacings observed by HRTEM (Figure 1f). Concave F:In_2O_3 cubes (1 and 2% InF_3) are also single crystalline, as observed in SAED patterns collected down the ⟨100⟩ zone axis (Figure 1d,e right). An HRTEM image of the elongated tip on a concave cube (1% InF_3) shows (022) lattice spacing (3.56 Å), along with (400) lattice spacing parallel to the facets (Figure 1g). Together, these observations indicate that the as-synthesized F:In_2O_3 cubes have cubic bixbyite {100}-dominant surface facets.

To quantify total fluorine incorporation in F:In_2O_3 NCs (Table 1), EDX spectroscopy (Figure S3) and TOF-SIMS

DOI: 10.1021/acs.chemmater.9b00906
Chem. Mater. 2019, 31, 2661−2676

analysis were conducted (Figure S4). Because the emitted X-rays are of high energy, EDX has an effective probe depth of about 200 nm; the entire volume of the NCs is probed, and the results approximately reflect the overall F/In atomic (at.) composition ratio. However, owing to the low sensitivity of EDX to fluorine in the low-dopant-concentration NC samples, (e.g., 1% InF_3), TOF-SIMS was employed to quantify the F/In atomic ratio as a film of NCs was progressively etched. Both EDX and TOF-SIMS support a trend of increasing F atomic composition in $F:In_2O_3$ NCs as a function of InF_3 concentration employed during synthesis. Lower F/In was observed in 12% InF_3 when compared with the initial F/In, suggesting fluorine saturation within the NC lattice under excessive addition of dopant precursor. Syntheses with $InCl_3$ and $InBr_3$ precursors were observed to result in low halide (X = Cl, Br) incorporation instead.

Aliquots taken during the synthesis of $F:In_2O_3$ cubes (3% InF_3) were analyzed by FTIR spectroscopy to assess the chemical decomposition mechanism. Typically, $In(acac)_3$ and oleic acid were heated at 120 °C to form an indium oleate (In-OA) precursor. For $F:In_2O_3$ NCs, a ramp rate of 15 °C/min to 320 °C was used to rapidly decompose the indium precursors. In-OA and octylamine (OcAm) lead to the formation of indium monomers and amide by-products[44,45] (Figure S5). The FTIR fingerprint region shows that the precursor undergoes an aminolysis reaction with OcAm during synthesis. The metal carboxylate (1614 and 1582 cm^{-1}) peak signals[46,47] are significantly reduced in intensity after heating to 260 °C and continue to fall as the reaction progresses from 0 to 5 min, past this point. Concurrently, amide by-product C═O stretching (1688 cm^{-1}) and N−H bending (1651 cm^{-1}) signals[48,49] increase as In-OA is decomposed (Figure S5). These observations indicate that aminolysis is a primary mechanism of growth, which entails nucleophilic attack of the alkylamine on the metal−alkylcarboxylate complex, which is a common NC growth mechanism for metal oxides.[50,51] An aliquot taken during decomposition at 280 °C showed small irregularly shaped particles indicative of aggregative nucleation (Figure S5).[52] Irregular nuclei cohere together through oriented attachment, as observed in HRTEM, resulting in large sized NC seeds. Average NC product yield was 54.3% by weight for all $F:In_2O_3$ NC samples. Differing from typical doped In_2O_3 NC syntheses,[53] such large sized (100 nm scale) NCs are enabled by a combination of aminolysis-driven growth, aggregative nucleation, and a concentrated precursor solution (0.2 mmol/mL) at a high reaction temperature (320 °C).

To evaluate the progression of NC shape with reaction time, SEM analyses were performed on aliquots collected during the growth of $F:In_2O_3$ cubes. As reaction time progresses and the precursors progressively decompose, NC size is expected to increase, accompanied by either shape retention or changes. Aliquots taken during the growth of $F:In_2O_3$ cubes (3% InF_3) show that the cube morphology is retained throughout the 5 min growth period (Figure 2a) as size increases from 35.6 ± 7.6 to 81.6 ± 11.4 nm (Figure 2b). This indicates {100} surface stabilization throughout growth at sufficient InF_3 concentration, allowing synthesis of well-defined cube-shaped NCs. The cubic morphology was established after an initial nuclei aggregation phase as irregular aggregates became cubic during growth. Aliquots over longer reaction times (at 5 min, 30 min, 1 h, and 2.5 h) at 320 °C were also taken to observe the morphology evolution. At extended reaction times, corner rounding was observed. At longer reaction times of 2.5 h or more, the well-defined edge and corner morphology becomes a truncated cube with the appearance of {111} facets at the cube edges (Figure S6). At even longer growth times, pitting is apparent on the {100} facets, potentially due to corrosion by F^- ions or their reaction by-products.[14,15]

For the concave $F:In_2O_3$ cubes (1% InF_3), SEM images of aliquots reveal progressive growth at the corners that results in morphological evolution (Figure 2c). The initial aliquot, taken when turbidity was first observed in the reaction flask (0 min), shows cube-shaped NCs that are 81.3 ± 15.3 nm in size. SEM images show a second stage involving rapid NC size growth (Figure 2d) and observation of ledges on the faces. In the final stage, ledges converge into elongated tip extensions that project in the ⟨111⟩ directions, from the corners. A smooth concave surface has replaced the flat {100} cube facets in the final 5 min aliquot to form 274.0 ± 45.5 nm sized $F:In_2O_3$ concave cubes with elongated corners. This suggests that the {100} facets may not be as stable for this case, compared with the cubes synthesized with 3% InF_3 in the reaction mixture. At longer reaction times of 2.5 h or more, further rounding of the elongated corners occurs (Figure S6).

The synthesis of well-defined $F:In_2O_3$ cubes was also found to depend on the reaction temperature. For the 3% InF_3 synthesis, which produced optimally structured cubes at 320 °C, the morphological evolution was studied for reactions at temperatures between 280 and 340 °C. Strongly faceted cube shapes were produced at reaction temperatures of 340 and 320 °C (Figure S6). However, at a lower reaction temperature (280 °C), smaller rounded cubes were observed after 5 min of reaction time, evolving after 30 min to more defined cubic shapes.

The concave cube morphology is more sensitive to reaction temperature. Synthesizing $F:In_2O_3$ NCs (1% InF_3) at an elevated reaction temperature (340 °C) resulted in irregular pseudospherical shapes with growth in randomly oriented directions (Figure S6). Apparently, the preference for growth in the ⟨111⟩ direction is weakened at higher growth temperatures, which is consistent with growth occurring without directional preference potentially due to enhanced monomer diffusion along the surface at high temperatures.[54] Synthesizing $F:In_2O_3$ NCs (1% InF_3) at a lower reaction temperature (280 °C) resulted in rounded NCs instead of a concave cube morphology, up to 2.5 h of reaction time (Figure S6).

Influences of Fluorine on NC Shape. SEM and HRTEM analyses indicate that fluorine has a facet-directing function in the growth of $F:In_2O_3$ NCs. The cube-shaped NCs were produced only in the presence of fluorine (Figure 1a, right), whereas the cubic shape is not observed in its absence (Figure 1a, left). To assess whether fluorine is unique compared with other halides as a morphology-directing agent under these synthesis conditions, $InCl_3$ and $InBr_3$ were used in place of InF_3. The bond dissociation energy is 439 kJ/mol for the In−Cl bond and 418 kJ/mol for the In−Br bond, which are lower than that for In−F at 506 kJ/mol.[55] In−F bonds, being stronger than In−O bonds (at 360 kJ/mol), are hypothesized to be highly stable at In_2O_3 NC surfaces, whereas weaker In−Cl or In−Br bonds are less favorable due to lower electronegativity than that of fluorine and differing ionic radii (Cl^-: 1.81 Å and Br^-: 1.96 Å) causing strain when substituting surface oxygen (O^{2-}: 1.28 Å).[14,56] The NC products synthesized in the presence of $InCl_3$ or $InBr_3$ were large and rounded: 246.7 ± 16.6 nm for Cl:In_2O_3 NCs and 348.3 ± 58.1 nm for Br:In_2O_3 NCs with poorly defined facets (Figure S7), whereas F:In_2O_3 cubes synthesized with the same precursor ratio had well-defined shapes with edge lengths of 162.1 ± 9.2 nm (Figure S1).

Since fluorine plays an important role in the faceting of the In_2O_3 NCs, XPS was used to probe the presence of fluorine on their surfaces. XPS is sensitive to surface composition, since the escape depth of photoelectrons is only a few nanometers. The existence of fluorine on the F:In_2O_3 NC surfaces was revealed by XPS spectra acquired for the In 3d (Figure 3a) and F 1s (Figure 3b) regions. As shown in Figure 3a, the In $3d_{5/2}$ signal was deconvoluted into components that are assignable to lattice In−O (444.3 eV), In−OH (445.0 eV), and In−F (445.8 eV) species,[57] with the peak due to the In−F species becoming more dominant as the InF_3 precursor concentration is increased. Furthermore, the F 1s peak at 684.6 eV, flanked by the In 3p doublet peaks, also exhibits an increase in relative intensity as the InF_3 precursor concentration is increased (Figure 3b). Deconvolution of the O 1s signal is shown in Figure S8, with components that are assignable to lattice oxygen (530.0 eV), oxygen adjacent to oxygen vacancies, or other charged defects, such as $F_O^{\bullet}$ (531.0 eV), surface hydroxyl (531.8 eV), and carboxyl (533.1 eV) species, respectively.[57] Overall, the undoped In_2O_3 NCs are observed to have more surface-adsorbed hydroxyl and carboxyl species, as compared to F:In_2O_3 NCs, which further signifies the incorporation of F species as surface-capping agents. XPS characterization thus suggests that fluorine adsorbs on the In_2O_3 NC surfaces, which may be linked to the stability and prevalence of {100} facets in cube-shaped NCs.

Fluoride anions have been described as facet-directing agents in metal oxide NCs,[14] such as in the fluorinated synthesis of TiO_2 NCs,[21,56] and may also have played this role in the synthesis of F and Sn co-doped In_2O_3 NCs.[20] Metal fluoride precursors, such as InF_3, decompose into HF in the presence of oleic acid during the reaction, releasing fluoride anions and passivating the In−O surfaces with In−F bonds.[21] Walsh et al.[58] determined through density functional theory (DFT) calculations that for bixbyite In_2O_3, relaxed {111} facets are energetically preferred over oxygen-terminated {100} facets ($\gamma_{(111)} < \gamma_{(100)}$). However, surface passivation by F^- in metal oxide NCs can be expected to alter the energetic sequence of the facets: F^- passivation of the {100} facets results in surface energy inversion ($\gamma_{(111)} > \gamma_{(100)}$).[56] Correspondingly, F^- functions as a favorable {100} facet capping agent over {111} in the bixbyite In_2O_3 NCs, which we expect hinders growth at F^- terminated {100} surfaces due to fewer O sites available for In−OH monomer condensation to occur. We suggest that this directs the synthesis of well-defined F:In_2O_3 cube NCs (3% InF_3) wherein sufficient F^- passivation occurs at the {100} facets.

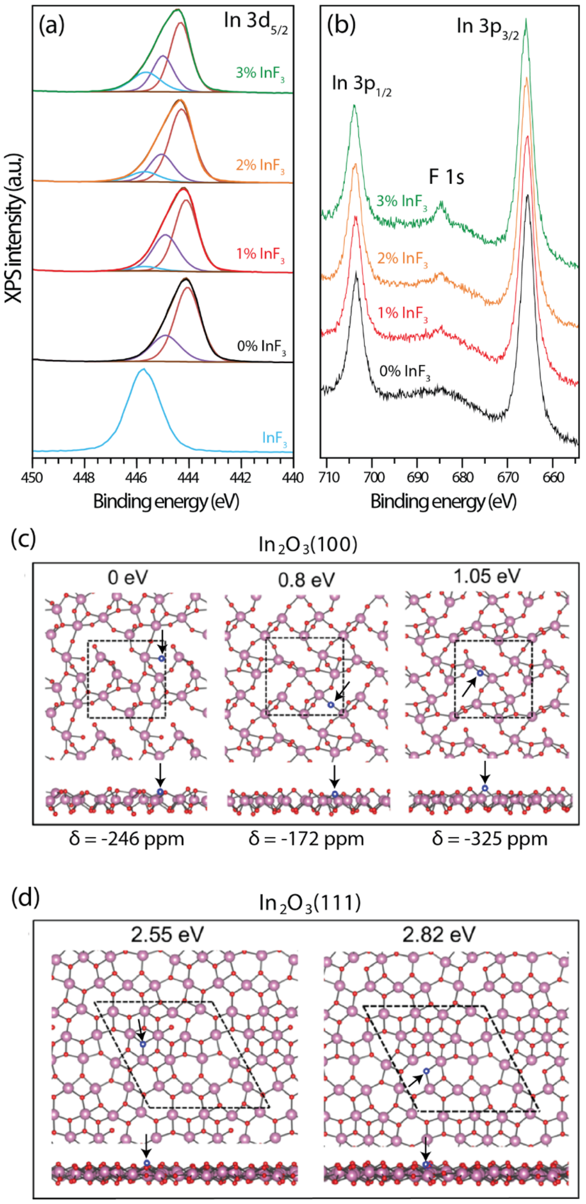

Figure 3. Rationalizing F incorporation in the F:In_2O_3 NCs by XPS and DFT. (a) In $3d_{5/2}$ XPS spectra showing the contributions of various components (red = In−O, purple = In−OH, and blue = In−F), and (b) F 1s (along with In 3p) XPS spectra for undoped In_2O_3 NCs (black curve), concave cubes (red curve), sharp concave cubes (orange curve), and cubes (green curve). Note that the In−F component (blue curve in panel (a)) increases in intensity as the InF_3 concentration used during synthesis is increased. In $3d_{5/2}$ spectrum for InF_3 is shown for reference (blue curve, bottom). DFT-calculated top and side views of an F atom substituting O on (c) (100) surface, and (d) (111) surface. Red: O; purple: In; blue: F (marked with arrows). For clarity, only the top In layer and the coordinated O and F are shown. The number on top of each panel shows the corresponding formation energy of the F/O substitution (see the Supporting Information) with respect to the most stable configuration (c, left). δ_{iso} is the calculated NMR isotropic chemical shift. Only low-energy structures for each surface are shown.

To understand the surface effects of fluorine on the morphology of In_2O_3, DFT calculations were conducted (details in Text S1, Supporting Information) by calculating relative formation energies of F substituting at surface O atomic sites on (100) and (111) surfaces. The (111) surface was selected for comparison with (100) as it has been reported to have the lowest surface energy in In_2O_3 without F doping.[58] All possible F substitution sites were considered, and only the low formation energy surface configurations are shown in Figure 3c,d. F substitution is more energetically favorable on the (100) surfaces than the (111) surfaces, with F substitution at (111) surfaces yielding formation energies (2.55, 2.82 eV) that are higher than the (100) surface configurations. Since growth through monomer deposition requires addition of new In and O atoms on oxygen-terminated sites,[59] it can be expected that this process is more difficult at fluorine-capped

(100) surfaces than on (111) surfaces. This explains why the (100) facets grow more slowly and become the dominant NC surface. NMR chemical shifts of ^{19}F atoms in different configurations on the (100) surface are calculated, with the most stable structure (Figure 3c, left) corresponding to a chemical shift of −246 ppm, to be compared below to experimental ^{19}F NMR spectra.

The complex concave cube shape of moderately passivated F:In_2O_3 NCs (1% InF_3) can be rationalized through the shape control model previously described for other halide-passivated NCs.[14,15] Colloidal syntheses of NCs involve both thermodynamic and kinetic effects that impact the NC shape. The conceptual framework involves two monomer addition processes: deposition on facets with high surface energy (kinetic) and monomer surface diffusion to minimize the total surface energy of NC facets (thermodynamic).[3] The high rate of In-OA precursor decomposition, driven by aminolysis, leads to a high rate of monomer deposition onto growth-favorable NC facets at a short reaction time (5 min). During fluorine-free synthesis, undoped In_2O_3 NCs exhibit growth in all ⟨100⟩, ⟨110⟩, and ⟨111⟩ directions into irregularly shaped NCs (Figure 1a, leftmost panel). With intermediate InF_3 concentrations (1−2% InF_3), the {100} facets are partially capped by F^-, and In monomer deposition becomes unfavorable on {100} facets with more F^- capped sites. Instead, the reaction conditions are favorable for selective monomer deposition on the less F^- surface occupied {111} facets. Thus, F^- passivated {100} facets have slower growth and monomers preferentially deposit on {111} facets during NC growth.[60] Through this process, elongated ⟨111⟩ direction tips are seen in F:In_2O_3 concave cube NCs (1% InF_3), with concave {100} facets (Figure 1a, second from left). Well-defined concave cube F:In_2O_3 NCs of 290.4 ± 17.9 nm size with sharp elongated ⟨111⟩ corners result when using a 2% InF_3 precursor content, showing distinct high-index quadrant boundaries on the {100} facets (Figure 1a, second from right). With higher InF_3 concentration (3% InF_3), the {100} facets become increasingly passivated by F^- capping, fluorine-terminated {100} surface exposure is favored for minimizing the total surface energy, and well-defined cube-shaped NCs result.

Since metal oxide NC growth through monomer deposition requires addition of new In and O atoms on oxygen-terminated sites, the observed NC growth in higher InF_3 precursor ratio reaction is expected to be slower due to fluorine termination on the NC surfaces. This slower growth leads to the smaller NC size in 3% InF_3 compared to that in 1% InF_3 throughout the growth aliquot observed in Figure 2. Due to aggregative nucleation,[52] we rationalize that the aggregative nuclei is also less prone to cohesion due to fluorine passivation of the oxygen-terminated NC nuclei surface. A higher InF_3 precursor would lead to smaller sized seeds and indicate a larger number of nuclei. The NC aliquot size in Figure 2 (0 min in Figure 2) is smaller in 3% InF_3 growth (35.6 nm) compared to that in a lower level of 1% InF_3 precursor (81.8 nm).

Although the XRD and electron diffraction patterns indicate substantial long- and short-range lattice order in the F:In_2O_3 NCs, the nonstoichiometric distributions of fluorine species introduce significant and important complexity to the NC structures that govern their growth and optical properties. The types, distributions, and electronic environments of fluorine atoms in F:In_2O_3 NCs are established by solid-state ^{19}F MAS NMR analyses. The solid-state 1D ^{19}F MAS NMR spectrum of F:In_2O_3 NCs (3% InF_3) in Figure 4a reveals four resolved ^{19}F signals at 50, −50, −208, and −234 ppm, which are assigned on the basis of the 2D $^1H\{^{19}F\}$ NMR correlation spectrum and ^{19}F spin-lattice relaxation time analyses discussed below to ^{19}F nuclei in different types of chemical and electronic environments in the F:In_2O_3 NCs.

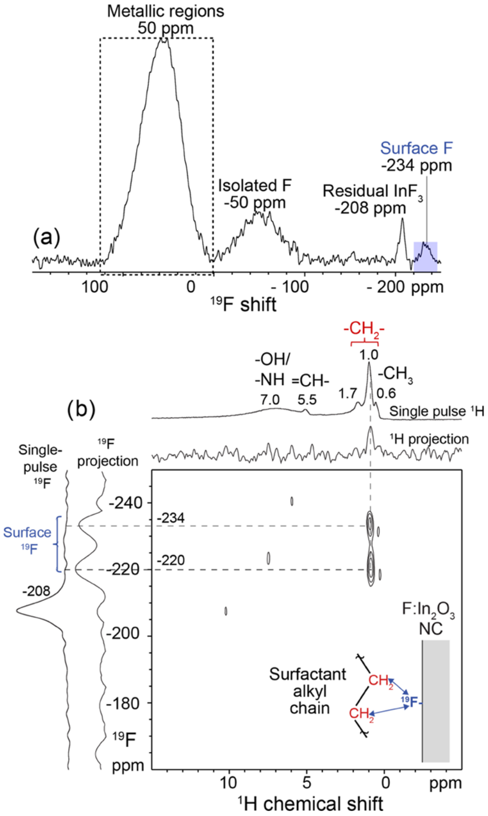

Figure 4. Solid-state (a) 1D ^{19}F echo and (b) 2D $^1H\{^{19}F\}$ correlation MAS NMR spectra of F:In_2O_3 NCs (3% InF_3) diluted in a 1:1 ratio by mass with KBr. Solid-state 1D single-pulse ^1H and ^{19}F spectra acquired under the same conditions are shown along the horizontal and vertical axes of the 2D spectrum in (b) for comparison with the 1D projections. The inset shows a schematic diagram of a surface ^{19}F moiety interacting with the alkyl chain of a surface-bound organic ligand, as indicated by arrows. The spectra were acquired at 9.4 T, (a) 35 kHz MAS and 395 K or (b) 25 kHz MAS and 327 K.

Importantly, dilute surface fluorine moieties are detected and identified in the solid-state two-dimensional (2D) $^1H\{^{19}F\}$ correlation NMR spectrum in Figure 4b. The spectrum is shown as a 2D contour plot, having ^1H and ^{19}F frequency axes (with units of ppm) on the abscissa and ordinate, respectively. Correlated signal intensities in the 2D spectrum arise only from ^1H species that are dipole−dipole-coupled with ^{19}F atoms over nanoscale distances (<0.5 nm for the short dipolar recoupling time, 0.96 ms, used here), thereby establishing the mutual proximities of the ^1H and ^{19}F species with associated signals. For comparison, a standard 1D ^1H MAS NMR spectrum is shown above the ^1H axis of the 2D spectrum, which exhibits signals at 0.6, 1.0, 1.7, 5.5, and 7.0 ppm that are all assigned to ^1H moieties on the octylamine, trioctylamine, or oleate organic surfactant molecules, as indicated by the labels above the respective ^1H signals. The 2D $^1H\{^{19}F\}$ correlation spectrum resolves two ^{19}F signals at −234 and −220 ppm that are correlated to ^1H signals at 1.0 ppm from $-CH_2-$ moieties on the organic surfactant molecules, unambiguously establishing the interactions and proximities of the corresponding ^1H

and ^{19}F species at the F:In_2O_3 particle surfaces. Notably, no correlated signal intensity is observed for the relatively narrow ^{19}F signal at −208 ppm (6 ppm full width half-maximum, FWHM), which is assigned to residual InF_3 precursor species.[61] Furthermore, whereas ^{1}H signal intensity is detected in 1D ^{1}H{^{19}F} NMR spectra acquired with ^{19}F excitation at −210 ppm, the same excitation frequency was used to acquire the 2D spectrum in Figure 4b, no ^{1}H signal intensity is detected for ^{19}F excitation at different frequencies (Figure S10). These results indicate that only the ^{19}F signals in the −220 to −234 ppm frequency range correspond to ^{19}F surface species and that the other types of ^{19}F environments detected in the 1D ^{19}F MAS NMR spectra in Figure 4a are located in subsurface environments, within the detection limits of the NMR measurements.

From the quantitative single-pulse 1D ^{19}F MAS NMR spectrum (Figure S11), the ^{19}F signals in the frequency range from −220 to −234 ppm account for only 1−2% of all the ^{19}F signal intensity, indicating that <2% of all of the ^{19}F species in the F:In_2O_3 NCs are in surface environments. These surface-related ^{19}F signals in the range of −220 to −234 ppm are close to the shift values predicted by DFT calculations for the most energetically stable ^{19}F structure on the (100) surface (−246 ppm, Figure 3c, left). Although the DFT models neglect other possible adsorbates for computational simplicity and represent an idealized subset of numerous possible surface configurations, this agreement suggests that the DFT calculations capture the main effects of fluorine on the (100) surface. The combined solid-state 1D ^{19}F and 2D ^{1}H{^{19}F} NMR analyses and DFT calculations thus identify and quantify the small fraction of ^{19}F species at the surfaces of the F:In_2O_3 NCs that are hypothesized to direct the NC morphology by adsorbing on (100) facet surface sites.

Fluorine as an Anionic Dopant. The discussion regarding fluorine has so far been limited to the NC surface: F^- selectively passivates NC surfaces to influence shape. The possible impact on the crystal lattice when F^- is incorporated into the In_2O_3 NCs is investigated by analyzing XRD as a function of fluorine incorporation. Fluorine being more electronegative than oxygen and the crystal ionic radius[62] of F^- (1.19 Å) being only slightly smaller than that of the O^{2-} site (1.28 Å) in bixbyite phase In_2O_3 would allow it to easily occupy oxygen sites.[19,63] XRD patterns (Figure S12) of F:In_2O_3 NCs (1−12% InF_3) confirm that the cubic bixbyite In_2O_3 crystal structure is maintained[64] and reveal that the F^- doping induces lattice strain. Lattice contraction relative to undoped In_2O_3 NCs is observed on the basis of the shift in the position of the (400) diffraction reflection at a low doping level (1% InF_3), which is ascribed to the smaller ionic radius of F^- as a substitutional dopant occupying O lattice sites not only at the surface but also internal to the NCs (Figure S12). Lattice contraction is also observed at low dopant concentrations in Sn:In_2O_3[65] and F:SnO_2,[63] where it has been similarly ascribed to aliovalent dopants with smaller ionic radii substituting the larger ions in host lattices. Rietveld refinement[33] of the full XRD pattern was conducted to quantify this initial lattice contraction and revealed the subsequent displacements of the (400) and (222) reflections at higher concentrations of F^- doping that correspond to lattice expansion (Figure S12). Size-induced lattice expansion or contraction, although reported in sub 10 nm metal oxide NCs, can be excluded due to the large size (100 nm or larger) of the In_2O_3 NCs considered here.[66] Undoped In_2O_3 NCs have a lattice constant of a = 10.126 Å, close to the reported bulk In_2O_3 value of a = 10.119 Å.[67] In low-doped 1% InF_3 concentration NCs, a contracted lattice constant of a = 10.083 Å was measured. However, lattice expansion occurs at higher dopant concentrations, similar to the structural changes reported in heavily doped F:SnO_2 and Sn:In_2O_3 films.[65,68] The (400) reflection shifts with F^- incorporation to a = 10.190 Å in 12% InF_3 doped NCs, resulting in a maximum observed lattice expansion of 0.58% that is attributed to dopant-screening effects from electrostatic repulsions.[65] Residual InF_3 is evident by XRD in the F:In_2O_3 NCs prepared with 3−12% InF_3 and can likely be attributed to emergent indium fluoride (InF_3) or indium oxyfluoride (InOF) residuals[69] (Figure S12).

To further understand the fluorine incorporation in the synthesized NC lattice, TGA was performed, as fluorine is known to diffuse out of NCs during high-temperature annealing under inert conditions.[70] TGA analysis shows initial weight loss starting at 400 °C that is ascribed to the removal of organic ligands. Upon further heating to 1100 °C, F:In_2O_3 cubes exhibit 1.3% weight reduction by fluorine liberation (Figure 5), corresponding to F/In = 9.6% atomic composition ratio. This TGA-based quantification agrees well with F/In = 10.3% quantified by TOF-SIMS. Concave F:In_2O_3 cubes show a 0.5% mass reduction corresponding to F/In = 3.7%, whereas undoped In_2O_3 NCs show little or no weight loss that could be associated with fluorine when heated to high temperatures. SEM images reveal the F:In_2O_3 cube NCs sinter into irregularly shaped massive particles during high-temperature annealing (Figure S13).

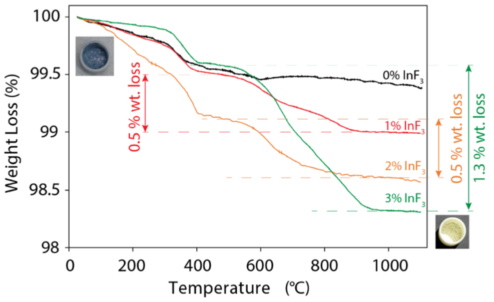

Figure 5. TGA curves for undoped In_2O_3 NCs (black curve), concave F:In_2O_3 cubes (red curve), sharp concave F:In_2O_3 cubes (orange curve), and F:In_2O_3 cubes (green curve). Photographs of the F:In_2O_3 cube sample (in an alumina crucible) before (left inset) and after TGA (right inset).

Substitutional fluorine dopants incorporated in the NCs can be charge-compensated by free electrons. Fluorine is well-established as an anionic n-type dopant that induces high free-electron concentrations in fluorine-doped tin oxide (F:SnO_2) transparent conductive oxide films.[22,63] The Kröger−Vink equation[71] for oxygen vacancy formation demonstrates that such defects in the In_2O_3 lattice can be charge compensated by two electrons (eq 1).[72] Oxygen substitution by F induces one free electron per fluorine ion (eq 2).[73,74]

$$\mathrm{In}_{\mathrm{In}}^{\times} + \mathrm{O}_{\mathrm{O}}^{\times} \rightarrow \mathrm{In}_{\mathrm{In}}^{\times} + V_{\mathrm{O}}^{\bullet\bullet} + 2e' + \frac{1}{2}\mathrm{O}_{2(g)} \qquad (1)$$

$$\mathrm{In}_{\mathrm{In}}^{\times} + 3\mathrm{O}_{\mathrm{O}}^{\times} \xrightarrow[\mathrm{InF}_3]{} 2\mathrm{In}_{\mathrm{In}}^{\times} + 3\mathrm{F}_{\mathrm{O}}^{\bullet} + 3e' + \frac{3}{2}\mathrm{O}_{2(g)} \qquad (2)$$

The band structure derived from DFT calculations predicts an elevated Fermi level when fluorine substitutes oxygen in In_2O_3, as compared to undoped In_2O_3. The Fermi level is calculated to be 1.1 eV above the conduction band minimum (Figure S14) with F dopants present in the In_2O_3 lattice unit cell (F/O = 1:47), due to free-electron carriers contributed to the conduction band, which leads to LSPR optical properties in F:In_2O_3 NC cubes. Electron paramagnetic resonance (EPR) spectroscopy provides evidence for free electrons in F:In_2O_3 NCs. The induced extra electrons are delocalized in the conduction band,[75,76] leading to an observed EPR signal at $g \approx 2.20$ in doped F:In_2O_3 cubes. By comparison, undoped In_2O_3 NCs exhibit a weak EPR signal at $g \approx 2.00$ due to a low population of oxygen vacancy-induced free electrons or shallow donors (Figure S15).[77,78] EPR spectra of the F:In_2O_3 cubes at cryogenic temperatures (100 K) showed increased signal intensity, which decreased at room temperature due to rapid free-electron relaxation.[79]

The Kröger−Vink notation suggests that halogen dopants with the same valency as F^- should contribute to free-electron compensation. However, the large ionic radii of chloride (Cl^-) or bromide (Br^-) suggests that they are not suitable dopants to incorporate in In_2O_3 NCs. Doping of Cl or Br atoms into In_2O_3 NCs was attempted to check the viability of other halogen dopants. EDX quantification showed very low halide incorporation for these NCs, as compared with F:In_2O_3 NCs synthesized at the same dopant precursor concentration (3% InX_3, X = F, Cl, Br) (Table 1). Cl:In_2O_3 NCs show only Cl/In = 0.32 ± 0.11% atomic composition ratio, and Br:In_2O_3 NCs had Br/In = 2.62 ± 0.06%, whereas F:In_2O_3 cubes show higher F/In = 11.76 ± 2.70%. The low anionic dopant concentration observed can be attributed to Cl^- (1.81 Å) having a much larger ionic radius than F^- (1.19 Å), which would yield a correspondingly large ionic radius mismatch (41.4%) with O^{2-} (1.28 Å) and cause significant lattice strain in the host lattice.[62] Similarly, Br^- (1.96 Å) is not incorporated within the In_2O_3 NC lattice, consistent with similar straining (53.1%).[62]

On the basis of quantitative 1D ^{19}F MAS NMR and ^{19}F spin-lattice relaxation time analyses, the majority of ^{19}F atoms in the F:In_2O_3 NCs are located in metallic subsurface environments. The 1D ^{19}F MAS NMR spectrum in Figure 4a shows two broad ^{19}F signals at 50 and −50 ppm with FWHM signal linewidths of 66 and 26 ppm, respectively. The ^{19}F signal at −50 ppm is similar to ^{19}F signals observed for some other metal oxyfluorides[80−82] and is assigned to isolated F^- anionic dopant species in the F:In_2O_3 NCs. By comparison, on the basis of temperature-dependent analyses of ^{19}F spin-lattice (T_1) relaxation times, the ^{19}F signal at 50 ppm is confidently assigned to a distribution of ^{19}F species in metallic environments in the F:In_2O_3 NCs. In metallic materials, including degenerately doped semiconductors,[83] nuclear spins and conduction band electrons in s-like orbitals couple through Fermi contact interactions. These interactions give rise to two characteristic effects that are manifested in the ^{19}F NMR spectra of F:In_2O_3 NCs: a frequency displacement of the ^{19}F NMR signals called the Knight shift[83−85] and a Korringa-type temperature dependence of the rate of ^{19}F nuclear spin-lattice relaxation.[84,86,87] For the ideal case of isolated nuclear spins coupled to a degenerate gas of electron spins, the Korringa contribution to the relaxation rate, $T_{1,K}{}^{-1}$, is related to the Knight shift, K, by the well-known Knight−Korringa relation[84,86]

$$T_{1,K}^{-1}(K,\ T) = \left(\frac{\gamma_n}{\gamma_e}\right)^2 \frac{4\pi k_B T}{\hbar} K^2 \tag{3}$$

where γ_n and γ_e are the gyromagnetic ratios of the nuclear and electron spins, respectively, k_B and $\hbar$ are the Boltzmann and Planck constants, and T is the absolute temperature. The Knight−Korringa relation shows that the $T_{1,K}{}^{-1}$ values for nuclear spins in metallic environments are proportional to both temperature, T, and the square of the Knight shift, K^2. Fluorine species in metallic environments may therefore be identified on the basis of analysis of the ^{19}F $T_1{}^{-1}$ values as functions of both NMR frequency position and temperature.

Analyses of the 1D ^{19}F MAS NMR spectra and $T_1{}^{-1}$ relaxation rates at temperatures of 276−395 K, shown in Figure 6, reveal that the broad ^{19}F signal at 50 ppm in Figure 4a corresponds to ^{19}F dopant atoms in metallic environments within the F:In_2O_3 NCs that exhibit Korringa-type relaxation behavior. By comparison, the ^{19}F signal at −50 ppm, which also manifests a broad distribution of ^{19}F environments, exhibits no Korringa-type temperature dependencies in its spin-lattice relaxation behavior, consistent with its assignment to a distribution of isolated ^{19}F dopants in the In_2O_3 lattice that experience chemical and/or paramagnetic shifts but not metallic Knight shifts. The ^{19}F frequency axis in Figure 4a is renormalized in Figure 6a such that the signal from isolated F^- dopant species (−50 ppm in Figure 4a) is set to a Knight shift K of 0 ppm. As shown in Figure 6a, the broad ^{19}F signal distribution at K = 100 ppm (50 ppm in Figure 4a) from ^{19}F species in metallic environments does not change significantly in width or position over the temperature range 276−395 K, consistent with the expected temperature invariance of Knight shifts for heavily doped semiconductors with the Fermi level above the conduction band minimum (Figure S14).[84] The ^{19}F $T_1{}^{-1}$ values were measured by ^{19}F saturation recovery experiments, and the $T_{1,K}$ values for each isochromat across the ^{19}F Knight-shifted signal distribution were extracted by subtraction of the temperature-independent contribution ($T_{1,0}{}^{-1}$) from the overall relaxation rate, $T_1{}^{-1}$

$$T_{1,K}^{-1}(K,\ T) = T_1^{-1}(K,\ T) - T_{1,0}^{-1} \tag{4}$$

The temperature- and shift-independent term $T_{1,0}{}^{-1}$ depends on the MAS rate and was measured to be 6.9 ± 0.3 s^{-1} at 25 kHz MAS and 4.8 ± 0.5 s^{-1} at 35 kHz MAS. Due to the MAS dependence of $T_{1,0}{}^{-1}$, this term likely reflects the contribution to the ^{19}F $T_1{}^{-1}$ relaxation rate of strong ^{19}F−^{19}F and/or ^{19}F−electron dipole−dipole couplings, which are partially averaged under MAS conditions. Additional details on the ^{19}F T_1 relaxation analyses and the extraction of the $T_{1,0}{}^{-1}$ and $T_{1,K}{}^{-1}$ terms are provided in the Supporting Information (Figure S16). The square root of the temperature-dependent relaxation term, $T_{1,K}{}^{-1/2}$, is plotted as a function of K for the K = 50−175 ppm region (the boxed region in Figure 4a) in Figure 6b. At temperatures of 395 K (red) and 276 K (blue), the measured $T_{1,K}{}^{-1/2}$ values show excellent agreement across the entire ^{19}F Knight shift distribution with the theoretical values predicted by the Knight−Korringa expression at the different temperatures (dotted lines), which notably has no adjustable parameters and is derived from first principles.[83,84,86] Additionally, the Knight−Korringa relation holds across the entire temperature range of 276−395 K. The Korringa-type plot in Figure 6c shows a plot of the $T_{1,K}{}^{-1}$ values extracted at the maxima of the ^{19}F Knight shift distribution (K = 100 ppm), as

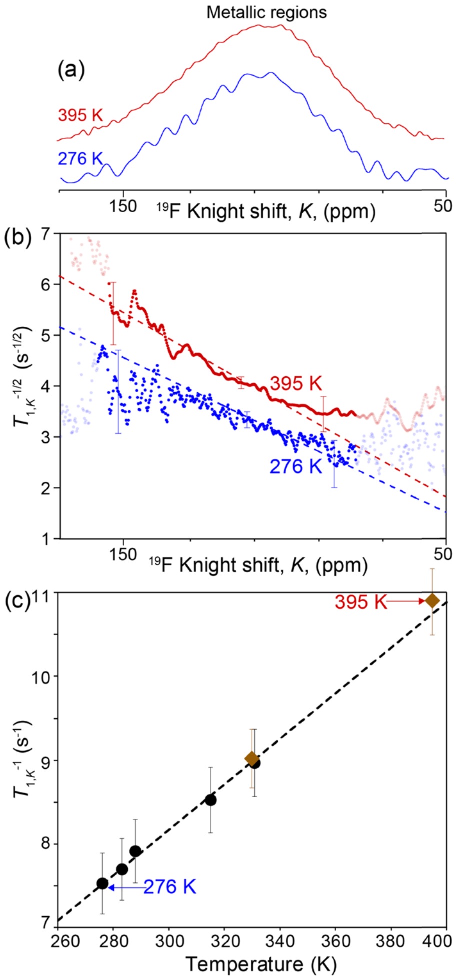

Figure 6. (a) Enlargement of the Knight-shifted ^{19}F spectral region (the boxed region in Figure 4a) showing a comparison of the 1D solid-state ^{19}F echo MAS NMR spectra of F:In_2O_3 NCs (3% InF_3) diluted in a 1:1 ratio by mass with KBr. The frequency axis is renormalized with the zero Knight shift peak at −50 ppm, corresponding to the signal from isolated F^- dopants in the F:In_2O_3 NCs. The spectra were acquired at 9.4 T at 35 kHz MAS and 395 K (red) and 25 kHz MAS and 276 K (blue). (b) Plot of the square root of the ^{19}F spin-lattice relaxation rate due to Korringa relaxation, $T_{1,K}^{-1/2}$, for different ^{19}F Knight shifts K in F:In_2O_3 NCs (3% InF_3), measured at 9.4 T at 35 or 25 kHz MAS and at 395 K (red) or 276 K (blue). Partially transparent data points correspond to spectral regions with little or no ^{19}F signal intensity, resulting in large uncertainties that are not pertinent to the analyses. (c) Plot of the ^{19}F $T_{1,K}^{-1}$ at the peak maximum of the Knight shift distribution (K = 100 ppm) as a function of temperature. Black circles and brown diamonds indicate $T_{1,K}^{-1}$ values measured under MAS conditions of 25 and 35 kHz, respectively. The dashed lines in (b) and (c) indicate theoretical values obtained from the Knight−Korringa equation (eq 3).

a function of temperature, revealing excellent agreement with the Knight−Korringa relation over the entire temperature range. This corroborates the conclusion that the broad ^{19}F signal at 50 ppm in Figure 4a arises from a distribution of Knight shifts that manifest a range of couplings of ^{19}F nuclei to conduction band electrons in regions of the F:In_2O_3 NCs with different extents of metallic character. The ^{19}F atoms, acting as anionic n-type dopants, therefore are sufficiently dense so that their associated unpaired electrons form a conductive network within the heavily doped In_2O_3 lattice.

Furthermore, on the basis of the quantitative single-pulse ^{19}F NMR spectrum of the F:In_2O_3 NCs (3% InF_3) (Figure S11), approximately 82 ± 1% of all of the ^{19}F species are in subsurface metallic environments in the In_2O_3 lattice, 17 ± 1% in residual InF_3, which is assigned on the basis of the XRD pattern and long ^{19}F relaxation time (23 s), and <1% at isolated dopant sites in the In_2O_3 lattice. The combined solid-state 2D ^{1}H{^{19}F} NMR correlation and ^{19}F T_1 relaxation analyses establish that only a small percentage (1−2%) of ^{19}F species are at the surfaces of the F:In_2O_3 NCs. The majority of ^{19}F species are incorporated into the F:In_2O_3 NCs in subsurface metallic domains, consistent with F^- as an anionic dopant within the In_2O_3 lattice.

The metallic domains are also manifested by evidence of conduction band electron influences on local ^{115}In environments in the F:In_2O_3 crystal lattice. Specifically, analyses and comparison of the solid-state wideline ^{115}In NMR spectra in Figure 7 of undoped bulk In_2O_3 and F:In_2O_3 NCs show differences that are characteristic of the coupling of ^{115}In nuclei to free electrons. Acquisition of solid-state ^{115}In NMR spectra has been exceedingly challenging in the past due to the highly quadrupolar character of ^{115}In nuclei (I = 9/2), which often exhibit very broad (several MHz) and poorly resolved ^{115}In NMR signals.[88] Very few solid-state ^{115}In NMR spectra of inorganic materials have been reported, with emphases primarily on materials with ^{115}In atoms in symmetric environments, such as cubic zinc blende semiconductors, like

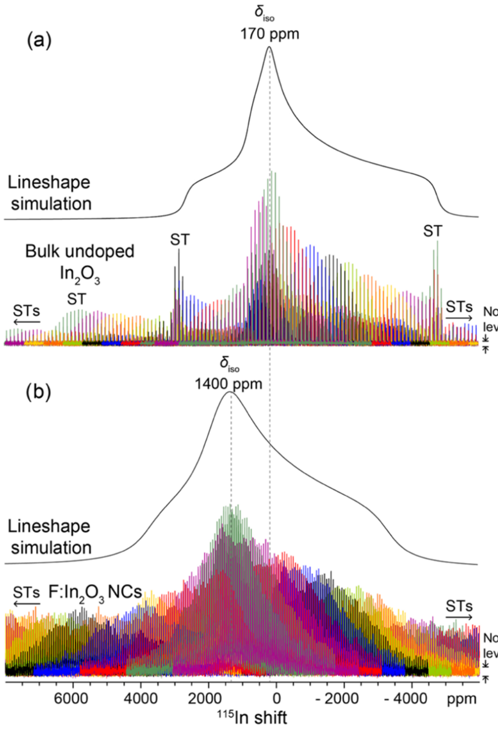

Figure 7. Solid-state 1D ^{115}In NMR spectra of (a) undoped microcrystalline In_2O_3 and (b) F:In_2O_3 NCs (3% InF) acquired at 295 K, under static conditions, and at magnetic field strengths of (a) 18.8 T and (b) 19.6 T. The spectra are an overlay of 22 different subspectra (shown as different colors) acquired at evenly spaced frequency intervals. Simulated ^{115}In NMR line shapes generated using the parameters in Table S1 are shown offset above the experimental ^{115}In NMR spectra. Signal intensities arising from ^{115}In satellite transitions are indicated by "ST."

InP and InN,[89,90] which yield narrower and more tractable line shapes. Nevertheless, recent wide line NMR techniques enable the detection and analysis of very broad NMR signals, even for quadrupolar nuclei in paramagnetic or conductive materials.[91−93]

Here, the frequency-stepped quadrupolar Carr−Purcell−Meiboom−Gill (QCPMG) technique[41] was used to measure the solid-state ^{115}In NMR spectra of bulk undoped polycrystalline In_2O_3 and F:In_2O_3 NCs (Figure 7). The QCPMG pulse sequence yields manifolds of very narrow, evenly spaced NMR signals (spikelets) that cannot cover the entire ^{115}In spectral range of these materials but can be systematically acquired as a series that can be overlain to map the full ∼2 MHz broad central transition (CT) region of the ^{115}In NMR spectrum. For example, the ^{115}In NMR spectrum in Figure 7a of bulk undoped In_2O_3 is presented as a mosaic overlay of 22 individual QCPMG subspectra (plotted in different colors) that were acquired at evenly spaced frequency intervals. Although a detailed analysis of the ^{115}In NMR line shapes is complicated by overlap of the numerous ^{115}In satellite transitions (STs) of the quadrupolar ^{115}In nuclei, the sensitivity and resolution of the wideline ^{115}In QCPMG spectra are sufficient to simulate the ^{115}In CT regions and estimate the quadrupolar coupling constant (C_Q), asymmetry parameter (η), and isotropic shift (δ_{iso}) for the bulk In_2O_3 (Table S1). Such NMR parameters are highly sensitive to the chemical and electronic environments of ^{115}In species in In_2O_3 and to our knowledge have never previously been measured or reported.

Compared with bulk In_2O_3, the ^{115}In NMR spectrum of F:In_2O_3 NCs is displaced and broadened, consistent with the coupling of ^{115}In nuclei to unpaired conduction band electrons. Both undoped polycrystalline In_2O_3 (Figure 7a) and F-doped In_2O_3 NCs (Figure 7b) exhibit very broad spectral features in the −4000 to 4000 ppm range that arise from the CT of ^{115}In nuclei in the different materials. The ^{115}In CT regions for both materials are reproduced by a single simulated ^{115}In lineshape with $C_Q \approx 130$ MHz and $\eta = 1$, although with different isotropic shifts (Figure 7, black spectra, see also Table S1). The bulk undoped In_2O_3 (cubic bixbyite phase by XRD, Figure S17) exhibits an isotropic ^{115}In shift of 170 ppm, consistent with diamagnetic ^{115}In environments in the In_2O_3 lattice. By comparison, the ^{115}In spectrum of F:In_2O_3 NCs (3% InF) exhibits an isotropic ^{115}In shift of 1400 ppm, displaced more than 1200 ppm from the position for diamagnetic In_2O_3. This displacement provides evidence that the majority of ^{115}In species in the F:In_2O_3 lattice experience substantial Knight shifts[83] arising from interactions with unpaired conduction band electrons associated with the F dopant species. The ^{115}In Knight shifts corroborate the ^{19}F NMR and T_1 spin-lattice relaxation time analyses discussed above. The ^{115}In NMR spectrum of the F:In_2O_3 NCs is also broadened compared to that of bulk undoped In_2O_3, indicating a larger distribution of chemical shifts, Knight shifts, and/or quadrupolar parameters (Table S1). The continuous distributions of signal intensity extending to higher and lower frequencies in both of the ^{115}In NMR spectra in Figure 7 arise from the very broad and overlapping ^{115}In satellite transitions, which are expected to span frequency regions of tens of MHz. To the best of our knowledge, the solid-state ^{115}In NMR spectra presented here are the first ^{115}In NMR analyses of In_2O_3, and evidence the sensitivity of ^{115}In NMR to different electronic environments in technologically important In_2O_3 materials.

In summary, the solid-state ^{19}F and ^{115}In NMR analyses together provide complementary and consistent evidence for metallic ^{19}F and ^{115}In environments in the heavily doped F:In_2O_3 lattice. Free electrons at the conduction band and spatially internal to F:In_2O_3 NCs interact with the nuclear spins of extrinsic dopant (F) and NC lattice (In) atoms. This gives rise to characteristic effects manifested in the NMR spectra of the degenerately doped semiconductors including ^{19}F and ^{115}In Knight shifts and Korringa-type temperature dependencies of the ^{19}F nuclear spin-lattice relaxation times.

Optical Properties. Considerations of charge compensation accompanying fluorine doping (eq 2) as well as the NMR analyses of the ^{19}F and ^{115}In species show that the anionically doped F:In_2O_3 NCs contain substantial free-electron populations leading to LSPR response. By eye, doped F:In_2O_3 NCs in solvent dispersions appear blue, in contrast to clear or white undoped In_2O_3 NCs (Figure S18). Liquid-cell FTIR spectra confirm that the F:In_2O_3 NCs exhibit IR range LSPR, with an absorption tail toward the visible region that is responsible for their blue appearance. The role of fluorine as an anionic dopant is apparent even in rounded F:In_2O_3 NCs (1% InF_3) synthesized at 280 °C. These NCs have a mean diameter of 338.0 ± 51.0 nm with 4.4 ± 0.4 atom % F by EDX, and exhibit an LSPR extinction peak at 3497 cm^{-1} (Figure 8). For comparison, undoped pseudospherical In_2O_3 NCs show a low-energy LSPR peak located at 1370 cm^{-1}, consistent with a low concentration of free electrons induced by the presence of oxygen vacancies (eq 1)[94] (Figure 8). In both Cl:In_2O_3 and Br:In_2O_3 NCs, however, the LSPR peak is at 1743 cm^{-1}, indicating low free-electron concentration compared to that of F:In_2O_3 NCs due to low dopant incorporation (Figure 8). These comparative observations demonstrate that fluorine is a uniquely effective anionic halide dopant for In_2O_3 NCs to induce LSPR in the IR region.

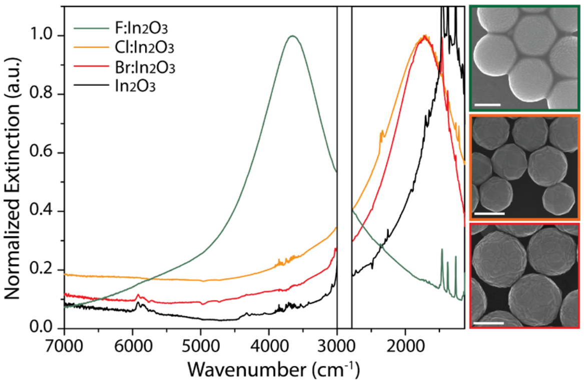

Figure 8. Liquid-cell FTIR spectra for spherical F:In_2O_3 (green line), Cl:In_2O_3 (orange line), Br:In_2O_3 (red line), and In_2O_3 NCs (black line). Spectral bands saturated by ligand absorption are shown as blank regions. (Inset) SEM images showing F:In_2O_3 (green), Cl:In_2O_3 (orange), and Br:In_2O_3 (red) NCs. Scale bars are 200 nm.

In the F:In_2O_3 cubes, the highly defined corners and edges are expected to result in multimodal LSPR extinction peaks in the IR spectral range. F:In_2O_3 cubes (3% InF_3) have highly pronounced plasmon peaks at 3496 cm^{-1} (FWHM 1157 cm^{-1}) and 5469 cm^{-1} (Figure 9a, green), respectively, ascribed to corner- and edge-dominated LSPR modes, by comparison to analogous modes observed for silver cubes.[95] Through the Drude model, the free-carrier density within the F:In_2O_3 cube

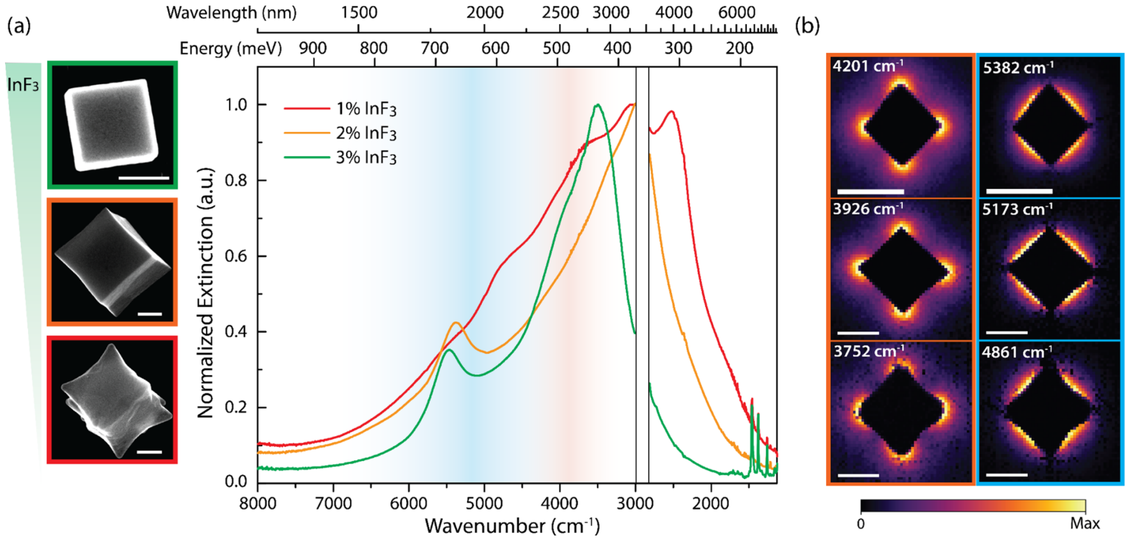

Figure 9. (a) Liquid cell FTIR spectra of $F{:}In_2O_3$ NCs with corresponding SEM images. $F{:}In_2O_3$ cube (green), $F{:}In_2O_3$ sharp concave cube (orange), and $F{:}In_2O_3$ concave cube (red). Scale bars are 100 nm. Spectral bands saturated by ligand absorption are shown as blank regions. Sharp peaks observed at 1000 cm^{-1} region are assigned to surface-bound organic ligands. (b) $F{:}In_2O_3$ (3% InF_3) cube (top), $F{:}In_2O_3$ (2% InF_3) sharp concave cube (middle), and $F{:}In_2O_3$ (1% InF_3) concave cube (bottom) EELS maps for corner mode frequencies (around 3900 cm^{-1}, left, orange) and edge mode frequencies (around 5100 cm^{-1}, right, blue) LSPR mode. Scale bars are 200 nm.

(3% InF_3) is estimated to be 6.8×10^{20} cm^{-3} on the basis of the LSPR extinction spectrum (Figure S19). Estimated from the NMR results, the concentration of F atoms in metallic environments in the $F{:}In_2O_3$ cubes is 2.5×10^{21} cm^{-3}, considering 80% of the F as being in a subsurface metallic environments and that the F/In atom ratio is 0.10. Combined, these estimates indicate that only a fraction of subsurface F atoms (27%) is activated and contributes electron carriers to the conduction band whereas the remainder of the internal F dopants are otherwise compensated.

Lower fluorine-doped $F{:}In_2O_3$ concave cube NCs exhibit changes in LSPR peak shape due to NC shape effects. Sharp concave cubes (2% InF_3) show well-defined modes with LSPR peaks at 2974 and 5378 cm^{-1} (Figure 9a, orange). Concave cubes (1% InF_3) with elongated ⟨111⟩ directional corners exhibit a complex LSPR response centered at 3030 cm^{-1} (Figure 9, red). Previous literature on plasmonic octopod Ag NCs has described the breakdown of simple cubic LSPR modes due to elongated corners.[96,97] By contrast, no multimode LSPR peaks are observed for rounded $F{:}In_2O_3$ NCs (1% InF_3) grown at 280 °C due to their mostly spherical shape (Figure 8, green).[10] During the growth of $F{:}In_2O_3$ NC cubes (3% InF_3), FTIR of aliquots demonstrate retention of both edge- and corner-mode LSPR peaks (Figure S20). The edge-mode LSPR at a higher wave number range is observed at 5690 cm^{-1} and retained during 1−4 min of reaction time. The corner-mode LSPR peak is also retained at 3340 cm^{-1} until the end of the growth reaction (2−4 min). It is observed that the $F{:}In_2O_3$ cube aliquot dopant composition is steady at F/In = 11.8 ± 0.4% throughout the growth reaction. This suggests that incorporation of subsurface fluorine species, as detected by ^{19}F NMR, is sustained during NC growth.

To definitively assign the contributions to the multimodal FTIR peaks observed in faceted $F{:}In_2O_3$ NCs, we perform STEM-EELS mapping of individual cubes. Optical LSPR excitation in the FTIR only allows ensemble far-field extinction measurements of cubes, where the incidence IR excitation wavelength (1250−10 000 nm) is within the LSPR quasistatic limit range.[10] The sub Angstrom diameter probe available in the STEM can directly sample and map the near-field localization of LSPR modes, and thanks to recent advances in monochromation, these mid-infrared frequencies are now accessible using EELS.[98,99] The spatial maps are acquired through spectrum imaging (SI), where the beam is rastered across the region of interest and a spectrum is acquired at each probe position, resulting in a three-dimensional dataset with two spatial dimensions and one spectral dimension. From here, individual plasmon modes are deconvoluted through the non-negative matrix factorization (NMF) method to produce spatially resolved EELS maps of individual LSPR modes.[95] For each structure, spatially and spectrally distinct corner and side modes can be observed and mapped through the deconvolved spectrum imaging, which are plotted in Figure 9b. The corner modes of $F{:}In_2O_3$ cube (3% InF_3), sharp concave cube (2% InF_3), and concave cube (1% InF_3) NCs are observed at 4201, 3926, and 3752 cm^{-1}, respectively, with the side mode resonances centered at 5382, 5173, and 4861 cm^{-1}. It is important to note that for the side modes, the NMF-deconvolution results in a spectral component with multiple peaks, likely corresponding to spatially overlapped edge and face modes. The reported peak center is the average of these face and edge modes. Details of the deconvolution and the EELS experiments are presented in greater detail in Text S3, Supporting Information.

Although FTIR samples the ensemble behavior and EELS samples individual structures, the match is strong enough to determine the modal nature of the FTIR peaks from the EEL-SI. The STEM analysis supports that the high-energy FTIR peaks correspond to the edge and face modes, whereas the lower energy peaks correspond to the corner modes. As in FTIR, in EELS the edge mode is observed at higher energy for the cube (3% InF_3) than for the sharp concave cube (2% InF_3). The frequencies of the corner modes do differ significantly between FTIR and EELS, which can be understood as originating from differences in the dielectric function in the liquid-cell FTIR experiments and the SiN/ultra-high-vacuum environment in the STEM.[100] The observed blue shift in the EELS mode relative to the FTIR spectrum is attributed to the lower refractive index ($n = 1$) of the surrounding vacuum in STEM, as compared with the TCE solution medium ($n = 1.5$) in the liquid-cell optical measurement.[101,102]

■ CONCLUSIONS

Fluorine plays a dual role as a dopant, influencing preferential growth of certain crystal facets and directing morphology of colloidally synthesized In_2O_3 NCs, as well as inducing IR range LSPR by aliovalent doping within the In_2O_3 NC lattice. In this study, we have demonstrated that introducing fluorine precursors in a typical heat-up method colloidal synthesis yields highly faceted F:In_2O_3 cube NCs with a shape-dependent LSPR response. Morphological control is demonstrated for the formation of concave cubes by adjusting the dopant concentration during F:In_2O_3 NC synthesis. Small percentages (1−2 atom %) of fluorine species are shown to be at the surfaces of the F:In_2O_3 NCs and hinder growth of {100} facets, as determined by combined XPS, solid-state 2D ^{1}H-{^{19}F} NMR and DFT analyses. By comparison, the majority of fluorine species are incorporated into subsurface metallic environments in the F:In_2O_3 lattice, consistent with F^- acting as an anionic dopant, as revealed by variable-temperature analyses of ^{19}F spin-lattice relaxation times and comparison to the Knight−Korringa relation. Complementary analyses of wideline ^{115}In NMR spectra show that the majority of ^{115}In species in the F:In_2O_3 species interact with unpaired conduction band electrons, providing corroboratory evidence that the F:In_2O_3 NC lattice is heavily doped beyond the metal-insulator transition. Arising from the combined effects of dopant-induced free carriers and highly faceted NC shapes, multimodal LSPR extinction features are observed in the IR. Single-NC LSPR near-field modes spatially localized around sharp morphological features are directly observed by STEM-EELS.

With this understanding of the role played by fluorine both on the NC surface and in the lattice, F:In_2O_3 NCs provide a valuable platform material for exploring properties and applications of LSPR-active NCs. Analogous to Ag nanocubes that exhibit visible LSPR,[95] well-defined In_2O_3 nanocubes are able to be colloidally synthesized, with shape-dependent LSPR in the IR spectral range. Near-field localization of IR light will make these highly faceted F:In_2O_3 NCs a platform material to evaluate near-field enhancement effects and explore applications unique to the infrared, including coupling LSPR to molecular vibrational modes[20] and IR emissive excitons.[103] To meet these demands, control of NC sizes and LSPR spectral tunability need be advanced. Large cube NC sizes lead to greater magnitude in near-field enhancement,[20] and full NC size control ranging from small to large cubes may allow a range of near-field intensities to be achieved. Further synthetic advances, such as the systematic incorporation of co-dopants,[19] may lead to additional LSPR tuning by increasing free-electron compensation in In_2O_3 NCs. However, synthetic questions remain as to fully understanding cationic co-dopant incorporation in metal oxides in the presence of anionic dopants.[20,104] The understanding of the dual role of fluorine as an anionic dopant in F:In_2O_3 NCs is expected to provide a foundation for addressing these questions and challenges and further improving the properties of these versatile materials.

■ ASSOCIATED CONTENT

Ⓢ Supporting Information

The Supporting Information is available free of charge on the ACS Publications website at DOI: 10.1021/acs.chemmater.9b00906.

> Details of nanocrystal characterization (SEM, EDX, TOF-SIMS, XPS, EPR, TGA, and XRD), nanocrystal aliquots (time and temperature series SEM, FTIR), solid-state NMR details (quantitative ^{19}F NMR, Knight−Korringa relation, ^{115}In simulated line shape parameters), DFT simulation (supercell, DFT calculation), and details of monochromated EELS (background subtraction, non-negative matrix factorization, and modal deconvolution) (PDF)

■ AUTHOR INFORMATION

Corresponding Authors

*E-mail: bradc@engineering.ucsb.edu (B.F.C.).
*E-mail: milliron@che.utexas.edu (D.J.M.).

ORCID

Shin Hum Cho: 0000-0002-0271-116X
Sandeep Ghosh: 0000-0002-1149-9199
Zachariah J. Berkson: 0000-0002-2157-4172
Jordan A. Hachtel: 0000-0002-9728-0920
Clayton J. Dahlman: 0000-0002-4555-4846
Yuanyue Liu: 0000-0002-5880-8649
Bradley F. Chmelka: 0000-0002-4450-6949
Delia J. Milliron: 0000-0002-8737-451X

Author Contributions

[#]S.H.C., S.G., and Z.J.B. contributed equally to this work.

Notes

The authors declare no competing financial interest.

■ ACKNOWLEDGMENTS

S.H.C., S.G., L.C.R., C.J.D, and D.J.M. acknowledge the support from the National Science Foundation (NSF, CHE-1609656, CBET-1704634, NASCENT, an NSF ERC—EEC-1160494, and CDCM, an NSF MRSEC—DMR-1720595), the Welch Foundation (F-1848), and Fulbright Program (IIE-15151071). We thank A. Dolocan, K. Jarvis, and H. Celio in the Texas Materials Institute (TMI) for user facility assistance. Y.L. and X.Z. acknowledge support from the Welch Foundation (Grant No. F-1959-20180324). Y.L. thanks the startup support from UT Austin. This work used computational resources sponsored by the Department of Energy (DOE), Office of Energy Efficiency and Renewable Energy located at the National Renewable Energy Laboratory (NREL) and the Texas Advanced Computing Center (TACC) at UT Austin. Z.J.B. was supported by a grant from the BASF Corporation. The solid-state NMR measurements made use of the MRL Shared Experimental Facilities of the University of California, Santa Barbara, which are supported by the MRSEC Program of the NSF under Award No. DMR 1720256; a member of the NSF-funded Materials Research Facilities Network (www.mrfn.org). We thank Drs. Z. Gan, I. Hung, and X. Wang for assistance with the solid-state ^{115}In NMR measurements of the F:In_2O_3 NCs conducted at the National High Magnetic Field Laboratory, which is supported by the National Science Foundation Cooperative Agreement No. DMR-1644779 and the State of Florida. Some microscopy research was performed as part of a user proposal at Oak Ridge National Laboratory's (ORNL) the Center for Nanophase Materials Sciences (CNMS), which is a U.S. Department of Energy, Office of Science User Facility (J.A.H., J.-C.I.). This research was conducted, in part, using instrumentation within ORNL's Materials Characterization Core provided by UT-Battelle, LLC, under contract No. DE-AC05-00OR22725 with the DOE. L.C.R. acknowledges the MMRRSA School at ORNL.

■ REFERENCES

(1) Agrawal, A.; Cho, S. H.; Zandi, O.; Ghosh, S.; Johns, R. W.; Milliron, D. J. Localized Surface Plasmon Resonance in Semiconductor Nanocrystals. *Chem. Rev.* **2018**, *118*, 3121−3207.

(2) Sasaki, T.; Endo, Y.; Nakaya, M.; Kanie, K.; Nagatomi, A.; Tanoue, K.; Nakamura, R.; Muramatsu, A. One-Step Solvothermal Synthesis of Cubic-Shaped ITO Nanoparticles Precisely Controlled in Size and Shape and Their Electrical Resistivity. *J. Mater. Chem.* **2010**, *20*, 8153−8157.

(3) Xia, Y.; Xia, X.; Peng, H.-C. Shape-Controlled Synthesis of Colloidal Metal Nanocrystals: Thermodynamic versus Kinetic Products. *J. Am. Chem. Soc.* **2015**, *137*, 7947−7966.

(4) Seo, D.; Park, J. C.; Song, H. Polyhedral Gold Nanocrystals with O_h Symmetry: From Octahedra to Cubes. *J. Am. Chem. Soc.* **2006**, *128*, 14863−14870.

(5) Zhou, S.; Li, J.; Gilroy, K. D.; Tao, J.; Zhu, C.; Yang, X.; Sun, X.; Xia, Y. Facile Synthesis of Silver Nanocubes with Sharp Corners and Edges in an Aqueous Solution. *ACS Nano* **2016**, *10*, 9861−9870.

(6) DeSantis, C. J.; Skrabalak, S. E. Size-Controlled Synthesis of Au/Pd Octopods with High Refractive Index Sensitivity. *Langmuir* **2012**, *28*, 9055−9062.

(7) Alvarez, M. M.; Khoury, J. T.; Schaaff, T. G.; Shafigullin, M. N.; Vezmar, I.; Whetten, R. L. Optical Absorption Spectra of Nanocrystal Gold Molecules. *J. Phys. Chem. B* **1997**, *101*, 3706−3712.

(8) Naik, G. V.; Shalaev, V. M.; Boltasseva, A. Alternative Plasmonic Materials: Beyond Gold and Silver. *Adv. Mater.* **2013**, *25*, 3264−3294.

(9) Luther, J. M.; Jain, P. K.; Ewers, T.; Alivisatos, A. P. Localized Surface Plasmon Resonances Arising from Free Carriers in Doped Quantum Dots. *Nat. Mater.* **2011**, *10*, 361−366.

(10) Agrawal, A.; Kriegel, I.; Milliron, D. J. Shape-Dependent Field Enhancement and Plasmon Resonance of Oxide Nanocrystals. *J. Phys. Chem. C* **2015**, *119*, 6227−6238.

(11) Kanehara, M.; Koike, H.; Yoshinaga, T.; Teranishi, T. Indium Tin Oxide Nanoparticles with Compositionally Tunable Surface Plasmon Resonance Frequencies in the Near-IR Region. *J. Am. Chem. Soc.* **2009**, *131*, 17736−17737.

(12) Buonsanti, R.; Llordes, A.; Aloni, S.; Helms, B. A.; Milliron, D. J. Tunable Infrared Absorption and Visible Transparency of Colloidal Aluminum-Doped Zinc Oxide Nanocrystals. *Nano Lett.* **2011**, *11*, 4706−4710.

(13) Gordon, T. R.; Paik, T.; Klein, D. R.; Naik, G. V.; Caglayan, H.; Boltasseva, A.; Murray, C. B. Shape-Dependent Plasmonic Response and Directed Self-Assembly in a New Semiconductor Building Block, Indium-Doped Cadmium Oxide (ICO). *Nano Lett.* **2013**, *13*, 2857−2863.

(14) Ghosh, S.; Manna, L. The Many "Facets" of Halide Ions in the Chemistry of Colloidal Inorganic Nanocrystals. *Chem. Rev.* **2018**, *118*, 7804−7864.

(15) Xia, X.; Xie, S.; Liu, M.; Peng, H.-C.; Lu, N.; Wang, J.; Kim, M. J.; Xia, Y. On the Role of Surface Diffusion in Determining the Shape or Morphology of Noble-Metal Nanocrystals. *Proc. Natl. Acad. Sci. U.S.A.* **2013**, *110*, 6669−6673.

(16) Liu, G.; Yang, H. G.; Pan, J.; Yang, Y. Q.; Lu, G. Q.; Cheng, H.-M. Titanium Dioxide Crystals with Tailored Facets. *Chem. Rev.* **2014**, *114*, 9559−9612.

(17) Meyns, M.; Iacono, F.; Palencia, C.; Geweke, J.; Coderch, M. D.; Fittschen, U. E. A.; Gallego, J. M.; Otero, R.; Juárez, B. H.; Klinke, C. Shape Evolution of CdSe Nanoparticles Controlled by Halogen Compounds. *Chem. Mater.* **2014**, *26*, 1813−1821.

(18) Ghosh, S.; Gaspari, R.; Bertoni, G.; Spadaro, M. C.; Prato, M.; Turner, S.; Cavalli, A.; Manna, L.; Brescia, R. Pyramid-Shaped Wurtzite CdSe Nanocrystals with Inverted Polarity. *ACS Nano* **2015**, *9*, 8537−8546.

(19) Ye, X.; Fei, J.; Diroll, B. T.; Paik, T.; Murray, C. B. Expanding the Spectral Tunability of Plasmonic Resonances in Doped Metal-Oxide Nanocrystals through Cooperative Cation−Anion Codoping. *J. Am. Chem. Soc.* **2014**, *136*, 11680−11686.

(20) Agrawal, A.; Singh, A.; Yazdi, S.; Singh, A.; Ong, G. K.; Bustillo, K.; Johns, R. W.; Ringe, E.; Milliron, D. J. Resonant Coupling between Molecular Vibrations and Localized Surface Plasmon Resonance of Faceted Metal Oxide Nanocrystals. *Nano Lett.* **2017**, *17*, 2611−2620.

(21) Gordon, T. R.; Cargnello, M.; Paik, T.; Mangolini, F.; Weber, R. T.; Fornasiero, P.; Murray, C. B. Nonaqueous Synthesis of TiO_2 Nanocrystals Using TiF_4 to Engineer Morphology, Oxygen Vacancy Concentration, and Photocatalytic Activity. *J. Am. Chem. Soc.* **2012**, *134*, 6751−6761.

(22) Avadhut, Y. S.; Weber, J.; Hammarberg, E.; Feldmann, C.; Schellenberg, I.; Pöttgen, R.; Schmedt auf der Günne, J. Study on the Defect Structure of SnO_2:F Nanoparticles by High-Resolution Solid-State NMR. *Chem. Mater.* **2011**, *23*, 1526−1538.

(23) Sherry, L. J.; Chang, S.-H.; Schatz, G. C.; Van Duyne, R. P.; Wiley, B. J.; Xia, Y. Localized Surface Plasmon Resonance Spectroscopy of Single Silver Nanocubes. *Nano Lett.* **2005**, *5*, 2034−2038.

(24) Hoang, T. B.; Akselrod, G. M.; Argyropoulos, C.; Huang, J.; Smith, D. R.; Mikkelsen, M. H. Ultrafast Spontaneous Emission Source Using Plasmonic Nanoantennas. *Nat. Commun.* **2015**, *6*, No. 7788.

(25) Hsu, S.-W.; Tao, A. R. Halide-Directed Synthesis of Square Prismatic Ag Nanocrystals by the Polyol Method. *Chem. Mater.* **2018**, *30*, 4617−4623.

(26) Hrelescu, C.; Sau, T. K.; Rogach, A. L.; Jäckel, F.; Feldmann, J. Single Gold Nanostars Enhance Raman Scattering. *Appl. Phys. Lett.* **2009**, *94*, No. 153113.

(27) Stiles, P. L.; Dieringer, J. A.; Shah, N. C.; Duyne, R. P. V. Surface-Enhanced Raman Spectroscopy. *Annu. Rev. Anal. Chem.* **2008**, *1*, 601−626.

(28) Coughlan, C.; Ibáñez, M.; Dobrozhan, O.; Singh, A.; Cabot, A.; Ryan, K. M. Compound Copper Chalcogenide Nanocrystals. *Chem. Rev.* **2017**, *117*, 5865−6109.

(29) Hsu, S.-W.; On, K.; Tao, A. R. Localized Surface Plasmon Resonances of Anisotropic Semiconductor Nanocrystals. *J. Am. Chem. Soc.* **2011**, *133*, 19072−19075.

(30) Sardar, K.; Deepak, F. L.; Govindaraj, A.; Seikh, M. M.; Rao, C. N. R. InN Nanocrystals, Nanowires, and Nanotubes. *Small* **2005**, *1*, 91−94.

(31) Palomaki, P. K.; Miller, E. M.; Neale, N. R. Control of Plasmonic and Interband Transitions in Colloidal Indium Nitride Nanocrystals. *J. Am. Chem. Soc.* **2013**, *135*, 14142−14150.

(32) Kim, J.; Agrawal, A.; Krieg, F.; Bergerud, A.; Milliron, D. J. The Interplay of Shape and Crystalline Anisotropies in Plasmonic Semiconductor Nanocrystals. *Nano Lett.* **2016**, *16*, 3879−3884.

(33) Toby, B. H.; Von Dreele, R. B. GSAS-II: The Genesis of a Modern Open-Source All Purpose Crystallography Software Package. *J. Appl. Crystallogr.* **2013**, *46*, 544−549.

(34) Kresse, G.; Furthmüller, J. Efficient Iterative Schemes for Ab Initio Total-Energy Calculations Using a Plane-Wave Basis Set. *Phys. Rev. B* **1996**, *54*, 11169−11186.

(35) Kresse, G.; Joubert, D. From Ultrasoft Pseudopotentials to the Projector Augmented-Wave Method. *Phys. Rev. B* **1999**, *59*, 1758−1775.

(36) Perdew, J. P.; Burke, K.; Ernzerhof, M. Generalized Gradient Approximation Made Simple. *Phys. Rev. Lett.* **1996**, *77*, 3865−3868.

(37) Monkhorst, H. J.; Pack, J. D. Special Points for Brillouin-Zone Integrations. *Phys. Rev. B* **1976**, *13*, 5188−5192.

(38) Yesinowski, J. P.; Ladouceur, H. D.; Purdy, A. P.; Miller, J. B. Electrical and Ionic Conductivity Effects on Magic-Angle Spinning Nuclear Magnetic Resonance Parameters of CuI. *J. Chem. Phys.* **2010**, *133*, No. 234509.

(39) Thurber, K. R.; Tycko, R. Measurement of Sample Temperatures under Magic-Angle Spinning from the Chemical Shift and Spin-Lattice Relaxation Rate of ^{79}Br in KBr Powder. *J. Magn. Reson.* **2009**, *196*, 84−87.

(40) Brouwer, D. H.; Kristiansen, P. E.; Fyfe, C. A.; Levitt, M. H. Symmetry-Based ^{29}Si Dipolar Recoupling Magic Angle Spinning NMR Spectroscopy: A New Method for Investigating Three-Dimensional Structures of Zeolite Frameworks. *J. Am. Chem. Soc.* **2005**, *127*, 542−543.

(41) Hung, I.; Rossini, A. J.; Schurko, R. W. Application of the Carr−Purcell Meiboom−Gill Pulse Sequence for the Acquisition of Solid-State NMR Spectra of Spin-1/2 Nuclei. *J. Phys. Chem. A* **2004**, *108*, 7112−7120.

(42) Krivanek, O. L.; Lovejoy, T. C.; Dellby, N.; Carpenter, R. W. Monochromated STEM with a 30 MeV-Wide, Atom-Sized Electron Probe. *Microscopy* **2013**, *62*, 3−21.

(43) Spiegelberg, J.; Idrobo, J. C.; Herklotz, A.; Ward, T. Z.; Zhou, W.; Rusz, J. Local Low Rank Denoising for Enhanced Atomic Resolution Imaging. *Ultramicroscopy* **2018**, *187*, 34−42.

(44) Narayanaswamy, A.; Xu, H.; Pradhan, N.; Kim, M.; Peng, X. Formation of Nearly Monodisperse In_2O_3 Nanodots and Oriented-Attached Nanoflowers: Hydrolysis and Alcoholysis vs Pyrolysis. *J. Am. Chem. Soc.* **2006**, *128*, 10310−10319.

(45) Pham, H. T.; Jeong, H.-D. Non-Monotonic Size Dependence of Electron Mobility in Indium Oxide Nanocrystals Thin Film Transistor. *Bull. Korean Chem. Soc.* **2014**, *35*, 2505−2511.

(46) Bronstein, L. M.; Huang, X.; Retrum, J.; Schmucker, A.; Pink, M.; Stein, B. D.; Dragnea, B. Influence of Iron Oleate Complex Structure on Iron Oxide Nanoparticle Formation. *Chem. Mater.* **2007**, *19*, 3624−3632.

(47) Nakamoto, K. *Infrared and Raman Spectra of Inorganic and Coordination Compounds: Part B: Applications in Coordination, Organometallic, and Bioinorganic Chemistry*; John Wiley & Sons, Inc.: Hoboken, NJ, 2008; Chapter 1, pp 1−273.

(48) Jin, Y.; Yi, Q.; Ren, Y.; Wang, X.; Ye, Z. Molecular Mechanism of Monodisperse Colloidal Tin-Doped Indium Oxide Nanocrystals by a Hot-Injection Approach. *Nanoscale Res. Lett.* **2013**, *8*, 153.

(49) Pavia, D. L.; Lampman, G. M.; Kriz, G. S.; Vyvyan, J. A. *Introduction to Spectroscopy*; Cengage Learning: Boston, MA, 2014.

(50) Zhang, Z.; Zhong, X.; Liu, S.; Li, D.; Han, M. Aminolysis Route to Monodisperse Titania Nanorods with Tunable Aspect Ratio. *Angew. Chem., Int. Ed.* **2005**, *44*, 3466−3470.

(51) Zhang, Z.; Lu, M.; Xu, H.; Chin, W.-S. Shape-Controlled Synthesis of Zinc Oxide: A Simple Method for the Preparation of Metal Oxide Nanocrystals in Non-Aqueous Medium. *Chem. − Eur. J.* **2007**, *13*, 632−638.

(52) Wang, F.; Richards, V. N.; Shields, S. P.; Buhro, W. E. Kinetics and Mechanisms of Aggregative Nanocrystal Growth. *Chem. Mater.* **2014**, *26*, 5−21.

(53) Lounis, S. D.; Runnerstrom, E. L.; Bergerud, A.; Nordlund, D.; Milliron, D. J. Influence of Dopant Distribution on the Plasmonic Properties of Indium Tin Oxide Nanocrystals. *J. Am. Chem. Soc.* **2014**, *136*, 7110−7116.

(54) Wang, Y.; He, J.; Liu, C.; Chong, W. H.; Chen, H. Thermodynamics versus Kinetics in Nanosynthesis. *Angew. Chem., Int. Ed.* **2015**, *54*, 2022−2051.

(55) Dean, J. A. *Lange's Handbook of Chemistry*; McGraw-Hill: New York, NY, 1992.

(56) Yang, H. G.; Sun, C. H.; Qiao, S. Z.; Zou, J.; Liu, G.; Smith, S. C.; Cheng, H. M.; Lu, G. Q. Anatase TiO_2 Single Crystals with a Large Percentage of Reactive Facets. *Nature* **2008**, *453*, 638−641.

(57) Karsi, N.; Lang, P.; Chehimi, M.; Delamar, M.; Horowitz, G. Modification of Indium Tin Oxide Films by Alkanethiol and Fatty Acid Self-Assembled Monolayers: A Comparative Study. *Langmuir* **2006**, *22*, 3118−3124.

(58) Walsh, A.; A. Catlow, C. R. Structure, Stability and Work Functions of the Low Index Surfaces of Pure Indium Oxide and Sn-Doped Indium Oxide (ITO) from Density Functional Theory. *J. Mater. Chem.* **2010**, *20*, 10438−10444.

(59) Jansons, A. W.; Plummer, L. K.; Hutchison, J. E. Living Nanocrystals. *Chem. Mater.* **2017**, *29*, 5415−5425.

(60) Khurshid, H.; Li, W.; Chandra, S.; Phan, M.-H.; Hadjipanayis, G. C.; Mukherjee, P.; Srikanth, H. Mechanism and Controlled Growth of Shape and Size Variant Core/Shell FeO/Fe_3O_4 Nanoparticles. *Nanoscale* **2013**, *5*, 7942−7952.

(61) Sadoc, A.; Biswal, M.; Body, M.; Legein, C.; Boucher, F.; Massiot, D.; Fayon, F. NMR Parameters in Column 13 Metal Fluoride Compounds (AlF_3, GaF_3, InF_3 and TlF) from First Principle Calculations. *Solid State Nucl. Magn. Reson.* **2014**, *59−60*, 1−7.

(62) Shannon, R. D. Revised Effective Ionic Radii and Systematic Studies of Interatomic Distances in Halides and Chalcogenides. *Acta Crystallogr., Sect. A: Found. Adv.* **1976**, *32*, 751−767.

(63) Ramaiah, K. S.; Raja, V. S. Structural and Electrical Properties of Fluorine Doped Tin Oxide Films Prepared by Spray-Pyrolysis Technique. *Appl. Surf. Sci.* **2006**, *253*, 1451−1458.

(64) Maruyama, T.; Nakai, T. Fluorine-doped Indium Oxide Thin Films Prepared by Chemical Vapor Deposition. *J. Appl. Phys.* **1992**, *71*, 2915−2917.

(65) Frank, G.; Köstlin, H. Electrical Properties and Defect Model of Tin-Doped Indium Oxide Layers. *Appl. Phys. A* **1982**, *27*, 197−206.

(66) Zhou, X.-D.; Huebner, W. Size-Induced Lattice Relaxation in CeO_2 Nanoparticles. *Appl. Phys. Lett.* **2001**, *79*, 3512−3514.

(67) Nadaud, N.; Lequeux, N.; Nanot, M.; Jové, J.; Roisnel, T. Structural Studies of Tin-Doped Indium Oxide (ITO) and $In_4Sn_3O_{12}$. *J. Solid State Chem.* **1998**, *135*, 140−148.

(68) Akkad, F. E.; Joseph, S. Physicochemical Characterization of Point Defects in Fluorine Doped Tin Oxide Films. *J. Appl. Phys.* **2012**, *112*, No. 023501.

(69) Costa, B. J.; Soufiane, A.; Messaddeq, Y. New Compositions of Fluoroindate Glasses with Higher Chemical Resistance. *Quim. Nova* **1998**, *21*, 370−371.

(70) Li, J.; Liu, C.; Ye, Y.; Zhu, J.; Wang, S.; Guo, J.; Sham, T.-K. Tracking the Local Effect of Fluorine Self-Doping in Anodic TiO_2 Nanotubes. *J. Phys. Chem. C* **2016**, *120*, 4623−4628.

(71) Kröger, F. A.; Vink, H. J. Relations between the Concentrations of Imperfections in Crystalline Solids. In *Solid State Physics*; Seitz, F., Turnbull, D., Eds.; Academic Press, 1956; Vol. 3, pp 307−435.

(72) Walsh, A. Surface Oxygen Vacancy Origin of Electron Accumulation in Indium Oxide. *Appl. Phys. Lett.* **2011**, *98*, No. 261910.

(73) Runnerstrom, E. L.; Kelley, K. P.; Sachet, E.; Shelton, C. T.; Maria, J.-P. Epsilon-near-Zero Modes and Surface Plasmon Resonance in Fluorine-Doped Cadmium Oxide Thin Films. *ACS Photonics* **2017**, *4*, 1885−1892.

(74) Seo, J.-S.; Jeon, J.-H.; Hwang, Y. H.; Park, H.; Ryu, M.; Park, S.-H. K.; Bae, B.-S. Solution-Processed Flexible Fluorine-Doped Indium Zinc Oxide Thin-Film Transistors Fabricated on Plastic Film at Low Temperature. *Sci. Rep.* **2013**, 3, No. 2085.

(75) Schimpf, A. M.; Ochsenbein, S. T.; Buonsanti, R.; Milliron, D. J.; Gamelin, D. R. Comparison of Extra Electrons in Colloidal N-Type Al^{3+}-Doped and Photochemically Reduced ZnO Nanocrystals. *Chem. Commun.* **2012**, *48*, 9352−9354.

(76) Schimpf, A. M.; Gunthardt, C. E.; Rinehart, J. D.; Mayer, J. M.; Gamelin, D. R. Controlling Carrier Densities in Photochemically Reduced Colloidal ZnO Nanocrystals: Size Dependence and Role of the Hole Quencher. *J. Am. Chem. Soc.* **2013**, *135*, 16569−16577.

(77) Zhang, L.; Yin, L.; Wang, C.; lun, N.; Qi, Y.; Xiang, D. Origin of Visible Photoluminescence of ZnO Quantum Dots: Defect-Dependent and Size-Dependent. *J. Phys. Chem. C* **2010**, *114*, 9651−9658.

(78) Whitaker, K. M.; Ochsenbein, S. T.; Polinger, V. Z.; Gamelin, D. R. Electron Confinement Effects in the EPR Spectra of Colloidal N-Type ZnO Quantum Dots. *J. Phys. Chem. C* **2008**, *112*, 14331−14335.

DOI: 10.1021/acs.chemmater.9b00906
Chem. Mater. 2019, 31, 2661−2676

(79) De Trizio, L.; Buonsanti, R.; Schimpf, A. M.; Llordes, A.; Gamelin, D. R.; Simonutti, R.; Milliron, D. J. Nb-Doped Colloidal TiO_2 Nanocrystals with Tunable Infrared Absorption. *Chem. Mater.* **2013**, *25*, 3383−3390.

(80) Yamakawa, N.; Jiang, M.; Key, B.; Grey, C. P. Identifying the Local Structures Formed during Lithiation of the Conversion Material, Iron Fluoride, in a Li Ion Battery: A Solid-State NMR, X-Ray Diffraction, and Pair Distribution Function Analysis Study. *J. Am. Chem. Soc.* **2009**, *131*, 10525−10536.

(81) Kiczenski, T. J.; Stebbins, J. F. Fluorine Sites in Calcium and Barium Oxyfluorides: F-19 NMR on Crystalline Model Compounds and Glasses. *J. Non-Cryst. Solids* **2002**, *306*, 160−168.

(82) Kiczenski, T. J.; Stebbins, J. F. The Effect of Fictive Temperature on the Structural Environment of Fluorine in Silicate and Aluminosilicate Glasses. *J. Am. Ceram. Soc.* **2006**, *89*, 57−64.

(83) Yesinowski, J. P. Solid-State NMR of Inorganic Semiconductors. In *Solid State NMR*; Chan, J. C. C., Ed.; Springer: Berlin, Heidelberg, 2012; pp 229−312.

(84) Yesinowski, J. P.; Berkson, Z. J.; Cadars, S.; Purdy, A. P.; Chmelka, B. F. Spatially Correlated Distributions of Local Metallic Properties in Bulk and Nanocrystalline GaN. *Phys. Rev. B* **2017**, *95*, No. 235201.

(85) Knight, W. D. Nuclear Magnetic Resonance Shift in Metals. *Phys. Rev.* **1949**, *76*, 1259−1260.

(86) Slichter, C. P. *Principles of Magnetic Resonance*, 3rd ed.; Springer: Berlin, Heidelberg, 1990.

(87) Korringa, J. Nuclear Magnetic Relaxation and Resonance Line Shift in Metals. *Physica* **1950**, *16*, 601−610.

(88) Zapart, W.; Zapart, M. B.; Zhukov, A. P.; Popolitov, V. I.; Shuvalov, L. A. Phase Transition in $In_3Sb_5O_{12}$ by NQR of ^{115}In Nuclei. *Phys. Lett. A* **1987**, *121*, 248−250.

(89) Han, O. H.; Timken, H. K. C.; Oldfield, E. Solid-state "Magic-angle" Sample-spinning Nuclear Magnetic Resonance Spectroscopic Study of Group III−V (13−15) Semiconductors. *J. Chem. Phys.* **1988**, *89*, 6046−6052.

(90) Jung, W.-S.; Han, O. H.; Chae, S.-A. Characterization of Wurtzite Indium Nitride Synthesized from Indium Oxide by In-115 MAS NMR Spectroscopy. *Mater. Lett.* **2007**, *61*, 3413−3415.

(91) Schurko, R. W. Ultra-Wideline Solid-State NMR Spectroscopy. *Acc. Chem. Res.* **2013**, *46*, 1985−1995.

(92) Pell, A. J.; Pintacuda, G. Broadband Solid-State MAS NMR of Paramagnetic Systems. *Prog. Nucl. Magn. Reson. Spectrosc.* **2015**, *84−85*, 33−72.

(93) Kim, J.; Ilott, A. J.; Middlemiss, D. S.; Chernova, N. A.; Pinney, N.; Morgan, D.; Grey, C. P. ^2H and ^{27}Al Solid-State NMR Study of the Local Environments in Al-Doped 2-Line Ferrihydrite, Goethite, and Lepidocrocite. *Chem. Mater.* **2015**, *27*, 3966−3978.

(94) Yin, P.; Hegde, M.; Tan, Y.; Chen, S.; Garnet, N.; Radovanovic, P. V. Controlling the Mechanism of Excitonic Splitting in In_2O_3 Nanocrystals by Carrier Delocalization. *ACS Nano* **2018**, *12*, 11211−11218.

(95) Nicoletti, O.; de la Peña, F.; Leary, R. K.; Holland, D. J.; Ducati, C.; Midgley, P. A. Three-Dimensional Imaging of Localized Surface Plasmon Resonances of Metal Nanoparticles. *Nature* **2013**, *502*, 80−84.

(96) Naumov, I. I.; Li, Z.; Bratkovsky, A. M. Plasmonic Resonances and Hot Spots in Ag Octopods. *Appl. Phys. Lett.* **2010**, *96*, No. 033105.

(97) Mulvihill, M. J.; Ling, X. Y.; Henzie, J.; Yang, P. Anisotropic Etching of Silver Nanoparticles for Plasmonic Structures Capable of Single-Particle SERS. *J. Am. Chem. Soc.* **2010**, *132*, 268−274.

(98) García de Abajo, F. J. Optical Excitations in Electron Microscopy. *Rev. Mod. Phys.* **2010**, *82*, 209−275.

(99) Hachtel, J. A.; Lupini, A. R.; Idrobo, J. C. Exploring the Capabilities of Monochromated Electron Energy Loss Spectroscopy in the Infrared Regime. *Sci. Rep.* **2018**, *8*, No. 5637.

(100) Li, G.; Cherqui, C.; Bigelow, N. W.; Duscher, G.; Straney, P. J.; Millstone, J. E.; Masiello, D. J.; Camden, J. P. Spatially Mapping Energy Transfer from Single Plasmonic Particles to Semiconductor Substrates via STEM/EELS. *Nano Lett.* **2015**, *15*, 3465−3471.

(101) Ringe, E.; DeSantis, C. J.; Collins, S. M.; Duchamp, M.; Dunin-Borkowski, R. E.; Skrabalak, S. E.; Midgley, P. A. Resonances of Nanoparticles with Poor Plasmonic Metal Tips. *Sci. Rep.* **2015**, *5*, No. 17431.

(102) Johns, R. W.; Bechtel, H. A.; Runnerstrom, E. L.; Agrawal, A.; Lounis, S. D.; Milliron, D. J. Direct Observation of Narrow Mid-Infrared Plasmon Linewidths of Single Metal Oxide Nanocrystals. *Nat. Commun.* **2016**, *7*, No. 11583.

(103) Akselrod, G. M.; Weidman, M. C.; Li, Y.; Argyropoulos, C.; Tisdale, W. A.; Mikkelsen, M. H. Efficient Nanosecond Photoluminescence from Infrared PbS Quantum Dots Coupled to Plasmonic Nanoantennas. *ACS Photonics* **2016**, *3*, 1741−1746.

(104) Cao, S.; Zhang, S.; Zhang, T.; Lee, J. Y. Fluoride-Assisted Synthesis of Plasmonic Colloidal Ta-Doped TiO_2 Nanocrystals for Near-Infrared and Visible-Light Selective Electrochromic Modulation. *Chem. Mater.* **2018**, *30*, 4838−4846.